

# ViEEG: Hierarchical Neural Coding with Cross-Modal Progressive Enhancement for EEG-Based Visual Decoding

Minxu Liu\*

liuminxu@nuaa.edu.cn

Nanjing University of Aeronautics  
and Astronautics  
Nanjing, China

Chunwei Tian

chunweitian@nwpu.edu.cn  
Northwestern Polytechnical  
University  
Xi'an, China

Donghai Guan†

dhguan@nuaa.edu.cn

Nanjing University of Aeronautics  
and Astronautics  
Nanjing, China

Chuhang Zheng

h.zheng@nuaa.edu.cn

Nanjing University of Aeronautics  
and Astronautics  
Nanjing, China

Qi Zhu‡

zhuqi@nuaa.edu.cn

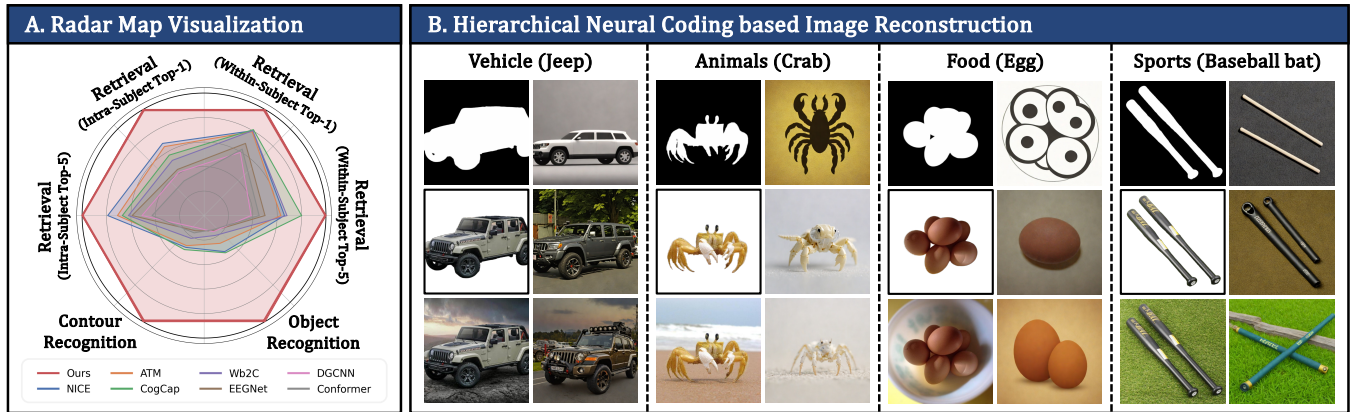
Nanjing University of Aeronautics  
and Astronautics  
Nanjing, China

Figure 1: EEG brain visual decoding of ViEEG.

## Abstract

Understanding and decoding brain activity into visual representations is a fundamental challenge at the intersection of neuroscience and artificial intelligence. While EEG-based visual decoding has shown promise due to its non-invasive, low-cost nature and millisecond-level temporal resolution, existing methods are limited by their reliance on flat neural representations that overlook the brain's inherent visual hierarchy. In this paper, we introduce ViEEG, a biologically inspired hierarchical EEG decoding framework that aligns with the Hubel-Wiesel theory of visual processing.

\*This author contributed equally to this work and is the first author.

†Corresponding author.

‡Corresponding author.

Permission to make digital or hard copies of all or part of this work for personal or classroom use is granted without fee provided that copies are not made or distributed for profit or commercial advantage and that copies bear this notice and the full citation on the first page. Copyrights for components of this work owned by others than the author(s) must be honored. Abstracting with credit is permitted. To copy otherwise, or republish, to post on servers or to redistribute to lists, requires prior specific permission and/or a fee. Request permissions from permissions@acm.org.

MM '25, Dublin, Ireland

© 2025 Copyright held by the owner/author(s). Publication rights licensed to ACM.

ACM ISBN 978-1-4503-XXXX-X/2018/06

<https://doi.org/XXXXXX.XXXXXXX>

ViEEG decomposes each visual stimulus into three biologically aligned components—contour, foreground object, and contextual scene—serving as anchors for a three-stream EEG encoder. These EEG features are progressively integrated via cross-attention routing, simulating cortical information flow from V1 to IT to the association cortex. We further adopt hierarchical contrastive learning to align EEG representations with CLIP embeddings, enabling zero-shot object recognition. Extensive experiments on the THINGS-EEG dataset demonstrate that ViEEG achieves state-of-the-art performance, with 40.9% Top-1 accuracy in subject-dependent and 22.9% Top-1 accuracy in cross-subject settings, surpassing existing methods by over 45%. Our framework not only advances the performance frontier but also sets a new paradigm for biologically grounded brain decoding in AI.

## CCS Concepts

- Human-centered computing → HCI theory, concepts and models;
- Computing methodologies → Hierarchical representations; Object recognition; Reconstruction.

## Keywords

Neuroscience Applications, Cognitive Science, Neural Decoding, Multimodal Learning, Zero-shot Learning, Image Reconstruction

### ACM Reference Format:

Minxu Liu, Donghai Guan, Chuhang Zheng, Chunwei Tian, Jie Wen, and Qi Zhu. 2025. ViEEG: Hierarchical Neural Coding with Cross-Modal Progressive Enhancement for EEG-Based Visual Decoding. In *Proceedings of Make sure to enter the correct conference title from your rights confirmation email (MM '25)*. ACM, New York, NY, USA, 24 pages. <https://doi.org/XXXXXXX>

## 1 Introduction

**Electroencephalogram (EEG)-based visual decoding** aims to bridge the gap between cortical dynamics and machine perception by reconstructing visual experiences from brain activity [8]. As a pivotal modality in brain-computer interfaces, EEG [7] has gained prominence due to its cost-effectiveness, portability, and millisecond-level temporal resolution. Recent years have witnessed substantial progress in EEG-based visual decoding methodologies [3, 8, 10, 20, 21, 31, 36, 40]. However, unlike functional magnetic resonance imaging (fMRI) signals [37] that have established sophisticated decoding frameworks [1, 15, 16, 24, 28, 33, 35, 39, 41], EEG-based visual decoding remains in its infancy, with significant challenges unaddressed, particularly in modeling the hierarchical visual processing mechanisms of the brain.

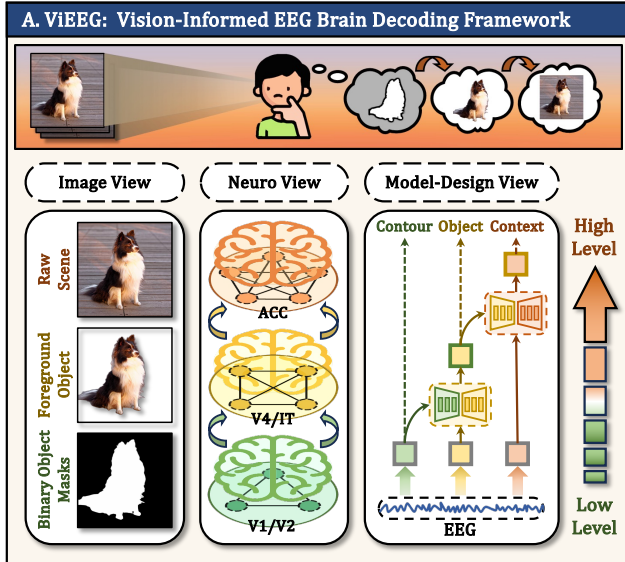


**Figure 2: Tri-View Hierarchical Framework for EEG-Based Visual Decoding.**

Contemporary EEG decoding approaches predominantly establish direct visual-semantic mappings between EEG signals and stimulus images. For instance, Wei et al. [36] employ contrastive learning for direct EEG-image embedding alignment with contrastive language-image pretraining (CLIP) [23, 25], while Song et al. [31] develop spatiotemporal neural architectures tailored for EEG visual decoding. Recent innovations include incorporating brain topological connectivity [20] and integrating multimodal semantic cues [40].

Despite these advancements, most existing methods overlook a fundamental property of the human visual system: its hierarchical nature. We term this issue as **Hierarchical Neural Encoding Neglect (HNEN)**. Rooted in the **Hubel-Wiesel model theory** [4], which established the canonical hierarchical cortical processing pathway, the human visual system processes stimuli through dissociable stages: from low-level edge detection to high-level semantic integration [9, 26]. In contrast, existing methods collapse this biological hierarchy into flat representation learning, resulting in incomplete visual information capturing.

Substantial neuroscientific evidence [4, 9, 19, 26] supports a hierarchically organized cortical visual pathway for visual perception: The early visual cortex (V1<sup>1</sup>/V2<sup>2</sup> [5]) specializes in elementary low-level feature extraction (e.g., edge contours), the intermediate ventral stream (V4<sup>3</sup>/IT<sup>4</sup> [2, 13]) processes object-level semantics, while higher-order association cortex correlates<sup>5</sup> [12] integrate high-level contextual scene understanding. This **hierarchical visual decoding** enables humans to progressively distill visual information—from coarse contours to fine-grained semantics—through layered cortical interactions. However, existing EEG-based brain decoding methods adopt a **monolithic processing paradigm** that adopts a flat representation paradigm that collapses biological hierarchy. By attempting direct mappings between EEG signals and holistic image embeddings, these approaches suffer from **HNEN**, failing to distinguish:

- Contour edge saliency (V1/V2 correlates)
- Foreground-object-centric semantics (V4/IT correlates)
- Contextual scene attributes (association cortex correlates)

The absence of **cortically-aligned feature disentanglement** fundamentally limits their capacity to localize visual saliency, particularly in preserving contour fidelity during EEG decoding.

Our proposed **vision-informed EEG (ViEEG)** brain decoding framework addresses HNEN through hierarchical visual decoding, as can be seen in Figure 2. We architect three complementary processing layers: (1) **Contour Priming Layer** where binary object masks guide EEG feature extraction for edge saliency, (2) **Object Purification Layer** that isolates foreground object semantics and purges background, and (3) **Contextual Integration Layer** capturing association cortex-level scene understanding from raw image. Three parallel spatiotemporal encoders decode EEG signals following the **hierarchical visual comprehension** (Contour → Object → Context), progressively integrating features through cross-attention mechanisms. The mask-constrained modules extract edge gradients, the object-centric attention refines core semantics, and the cross-stream fusion gates integrate contextual cues. Hierarchical CLIP anchoring reinforces biological plausibility: mask embeddings align with contour EEG patterns to preserve shape fidelity, object embeddings couple with foreground semantic features to suppress background interference, and raw image embeddings bind with contextual dynamics to maintain scene coherence. This structured mimicry of visual processing stages—from low-level edge detection to high-level semantic comprehension—directly resolves

<sup>1</sup>Primary visual cortex (V1): Edge processing

<sup>2</sup>Secondary visual cortex (V2): Edge processing

<sup>3</sup>Visual Area 4 (V4): Shape/color processing

<sup>4</sup>Inferotemporal Cortex (IT): Object recognition

<sup>5</sup>association cortex correlates (ACC): Scene context integration

the HNEN and flat representation bottleneck in conventional approaches through biologically-grounded feature disentanglement.

Our main contributions can be summarized as follows:

- **A biologically-inspired hierarchical framework** for EEG-based visual decoding, pioneering tri-stream modeling (Contour → Object → Context) aligned with cortical processing stages. To our knowledge, this is the first work to explicitly enforce feature disentanglement along the cortical hierarchy.
- **A novel cross-attention routing mechanism** that integrates multilevel EEG features via bottom-up hierarchical attention, enabling effective contour-object-contextual information fusion.
- **Bidirectional neuro-AI validation**, showing how neuroscientific theory can guide model design, while our decoding results, in turn, support biologically plausible brain representations.
- **New state-of-the-art performance** on THINGS-EEG: achieving 40.9% Top-1 ( $\uparrow 50\%$ ) in subject-dependent and 22.9% Top-1 ( $\uparrow 45\%$ ) in cross-subject settings, substantially outperforming previous benchmarks.

## 2 Related Works

### 2.1 Multimodal Learning

Human perception operates through intrinsically multimodal integration, where the brain dynamically synthesizes information across sensory and cognitive domains. This biological foundation has inspired computational frameworks that align neural activity with perceptual modalities such as vision and language. Recent advances attempt to decode brain signals into interpretable outputs. Recent advances have demonstrated the feasibility of translating brain activity into interpretable outputs, including neural speech synthesis [6], EEG-to-video generation [21], and EEG-based image reconstruction [31].

A dominant line of research leverages CLIP’s unified embedding space for cross-modal alignment. Mapping EEG signals into the CLIP space using InfoNCE-based contrastive learning has emerged as a standard strategy [20, 31, 36]. However, these approaches typically treat EEG as a holistic signal, overlooking the brain’s hierarchical structure in visual processing. In contrast, our method ViEEG incorporates biologically grounded visual decompositions—such as edge-based contours and background-free object entities—to preserve both low-level structure and high-level semantics. On the THINGS-EEG dataset, ViEEG achieves 40.9% Top-1 accuracy, surpassing CLIP-aligned flat decoders by nearly 50%, establishing a new biologically informed paradigm with improved interpretability and efficiency.

### 2.2 Brain Visual Decoding

Decoding the brain’s response to visual stimuli has been a central pursuit in neuroscience [4, 9, 19, 26] and brain-computer interface research [18, 29]. Early efforts predominantly focused on fMRI-based visual decoding [1, 16, 28, 33, 35], where high spatial resolution inherently captures hierarchical visual processing. For instance, Scotti et al. proposed MindEye [28], mapping fMRI signals to CLIP features via diffusion models, while Wang et al. developed MindBridge [35] to align fMRI with images and textual captions.

These methods leverage fMRI’s spatial precision to distinguish low-level (e.g., edges) and high-level (e.g., semantics) visual features implicitly, even when relying on simplistic fMRI-CLIP alignment.

In contrast, the spatial ambiguity of the EEG centimeter scale forces existing methods [8, 20, 24, 31, 36, 40] into flat representation paradigms that confuse hierarchical visual processing. As the dominant brain decoding approach of fMRI and EEG, direct EEG-image alignment fails to model the brain’s progressive refinement from edges to semantics, a limitation we term HNEN. While some attempts incorporate electrode topology [20] or depth cues [40], these merely address symptoms (e.g., spatial noise) rather than HNEN’s root cause: EEG’s inability to functionally isolate cortical processing stages.

This divergence highlights a critical gap: fMRI passively inherits hierarchical decoding through anatomy, whereas EEG demands active hierarchy simulation. Our proposed ViEEG bridges this gap via artificial cortical anchors—decomposing images into low-level edge masks (V1/V2 proxies), background-free entities (IT-level), and high-level contextual scenes (association cortex). By enforcing hierarchical EEG embedding disentanglement, we circumvent EEG’s spatial limitations while aligning with biological visual processing—a novel paradigm transcending both fMRI’s anatomy-dependence and EEG’s flat representations.

## 3 Preliminaries

In this section, we introduce the key notations used throughout the paper and formalize the task of EEG-based visual decoding.

### 3.1 Key Symbols

The core components of the proposed ViEEG framework are summarized in Table 1, where each symbol is defined based on both computational roles and neuroscientific alignment.

Symbol	Dim.	Definition
$E$	$\mathbb{R}^{C \times T}$	Raw EEG signals
$I$	$\mathbb{R}^{H \times W}$	Raw image
$I_b$	$\mathbb{R}^{D \times D}$	Binary object mask image
$I_f$	$\mathbb{R}^{D \times D}$	Foreground object image
$I_r$	$\mathbb{R}^{D \times D}$	Raw scene image
$F_b, F_f, F_r$	$\mathbb{R}^d$	Contour/object/context EEG embedding
$C_b, C_f, C_r$	$\mathbb{R}^d$	Contour/object/context CLIP embedding

**Table 1: Key symbol definitions with biological correspondences.**  $C$ : EEG channels,  $T$ : timepoints,  $H \times W$ : image resolution,  $D \times D$ : reshaped image resolution (512),  $d$ : embedding dimension (1024).

### 3.2 Task Formulation

We formulate EEG-based visual decoding as a hierarchical zero-shot object recognition task under an open-world assumption, where test categories are disjoint from the training set. Given EEG recordings  $E$  with  $N$  samples elicited by visual stimuli  $\{I_b, I_f, I_r\}$ , our objective is to learn hierarchical EEG embeddings  $\{F_b, F_f, F_r\}$  that align with

the corresponding CLIP embeddings  $\{C_b, C_f, C_r\}$  through hierarchical visual decoding. The learning objective for zero-shot object recognition is formulated as:

$$\min_{\theta} \frac{1}{N} \sum_{i=1}^N D(F^i, C^i), \quad (1)$$

where  $D(\cdot, \cdot)$  measures feature similarity. On the THINGS-EEG dataset, we train with class-disjoint stimuli and test on unseen categories. At inference time, the concatenated EEG embeddings  $F_b, F_f, F_r$  are compared to CLIP embeddings using cosine similarity within an InfoNCE-style contrastive learning framework [23].

## 4 Method

### 4.1 Overall Architecture

ViEEG introduces a biologically inspired hierarchical architecture for EEG-based visual decoding, simulating layered cortical processing. As illustrated in Figure 2, ViEEG comprises three synergistic components: (1) Hierarchical image decomposition, (2) Hierarchical EEG encoding, and (3) Hierarchical Contrastive Learning. During initialization, we extract CLIP embeddings from the three decomposed visual representations. In the training phase, Hierarchical EEG Encoding is employed to extract EEG features, which are then aligned with the image CLIP embeddings using Hierarchical Contrastive Learning. During testing, EEG embeddings extracted from the test set are matched to target samples based on similarity measurements for model evaluation.

### 4.2 Hierarchical Image Decomposition

Inspired by the hierarchical structure of the human visual system, as described in the classical Hubel-Wiesel model, we decompose each stimulus image  $I$  into three biologically aligned representations via semantic segmentation.

**Step 1: Image Processing.** We employ the pre-trained BiRefNet<sup>6</sup> [7], a state-of-the-art high-resolution segmentation model, to generate hierarchical visual representations. The raw image  $I$  is first normalized to yield  $I_r$ , ensuring consistent dimensions and intensity scaling. Saliency detection is then applied, and a binary contour representation is obtained via thresholding:

$$I_b = \mathbb{I}(\mathcal{F}_{\text{BiRefNet}}(I_r) > \tau) \quad (2)$$

where  $\mathcal{F}_{\text{BiRefNet}}$  denotes the pre-trained BiRefNet model,  $\mathbb{I}(\cdot)$  is the indicator function, and  $\tau$  is threshold value. The resulting  $I_b$  serves as a binary object mask that highlights salient contours. Next, to extract the foreground object, we perform element-wise multiplication:

$$I_f = I_r \odot I_b \quad (3)$$

where  $\odot$  denotes element-wise multiplication, and yielding  $I_f$ , the foreground object image with the background suppressed.

**Step 2: Image CLIP Embedding Processing.** To capture semantic information from each image representation, we utilize a frozen CLIP-ViT-H/14 to extract embeddings as follows:

$$C_b = \text{CLIP}(I_b), \quad C_f = \text{CLIP}(I_f), \quad C_r = \text{CLIP}(I_r) \quad (4)$$

<sup>6</sup><https://huggingface.co/ZhengPeng7/BiRefNet>

where  $C_b$ ,  $C_f$ , and  $C_r$  represent the embeddings corresponding to the binary mask, the foreground object, and the raw scene image, respectively. These embeddings serve as the foundation for subsequent hierarchical contrastive learning with EEG features.

### 4.3 Hierarchical EEG encoding

Our neuro-inspired encoding architecture extracts hierarchical (Contour/object/context) EEG features. Given raw EEG signals  $E$ , three parallel streams extract cortical hierarchy-aligned EEG features through spatiotemporal convolution (STConv) and cross-attention hierarchical integration (CAHI).

### 4.4 Spatiotemporal Convolution

To extract meaningful spatiotemporal representations from EEG signals, we employ a multi-stage convolutional processing pipeline. The first stage applies temporal convolution using a kernel of size  $(1, K_t)$  and a stride of  $S_t$ , capturing temporal dependencies across EEG signals. This is followed by an average pooling operation with a kernel size of  $(1, K_p)$  and a stride of  $S_p$ , which reduces temporal resolution while preserving crucial information. The second stage applies spatial convolution across electrodes using a kernel size of  $(C, 1)$ , performing spatial filtering. The processed features are then normalized and activated through an ELU function before being projected into the final hierarchical feature representation:

$$\begin{aligned} F^{(1)} &= \text{ELU}(\text{BatchNorm}(\text{AvgPool}(\text{Conv2D}_t(E)))) \\ F^{(2)} &= \text{ELU}(\text{BatchNorm}(\text{Conv2D}_s(F^{(1)}))) \\ F^{\text{init}} &= \text{Conv2D}_{\text{proj}}(F^{(2)}) \end{aligned} \quad (5)$$

where  $\text{Conv2D}_t(\cdot)$  denotes temporal convolution,  $\text{Conv2D}_s(\cdot)$  represents spatial convolution, and  $\text{Conv2D}_{\text{proj}}(\cdot)$  is a  $1 \times 1$  convolution. These hierarchical spatiotemporal features facilitate robust representation learning, which is further refined through the cross-attention mechanism. After three parallel STConv operations, EEG signals are decoupled into three features:  $F_b^{\text{init}}$ ,  $F_f^{\text{init}}$ , and  $F_r^{\text{init}}$ .

### 4.5 Cross-Attention Hierarchical Integration

The CAHI integrates biologically inspired features through contour-to-object and object-to-context feature integration. Since contour features can enhance existing object features, and object features provide additional context information, we integrate these two integration processes accordingly. Assuming that the low-level representation is denoted by  $a$  and the higher-level representation (object) by  $b$ , we perform bottom-up information integration, i.e., we transfer information from  $a$  to  $b$ . We use  $a$  and apply several linear transformations to generate the key embeddings for the attention mechanism, while  $b$  is used to generate the query and value embeddings:

$$K^i = a^i W^K, \quad Q^i = b^i W^Q, \quad V^i = a^i W^V \quad (6)$$

where  $a^i$  represents the  $i$ -th attention head, and  $W^Q$ ,  $W^K$ , and  $W^V$  are the parameter matrices for  $Q^i$ ,  $K^i$ , and  $V^i$ , respectively. We determine the attention coefficients by computing the scaled dot-product between  $Q$  and  $K$ , followed by a softmax to obtain the

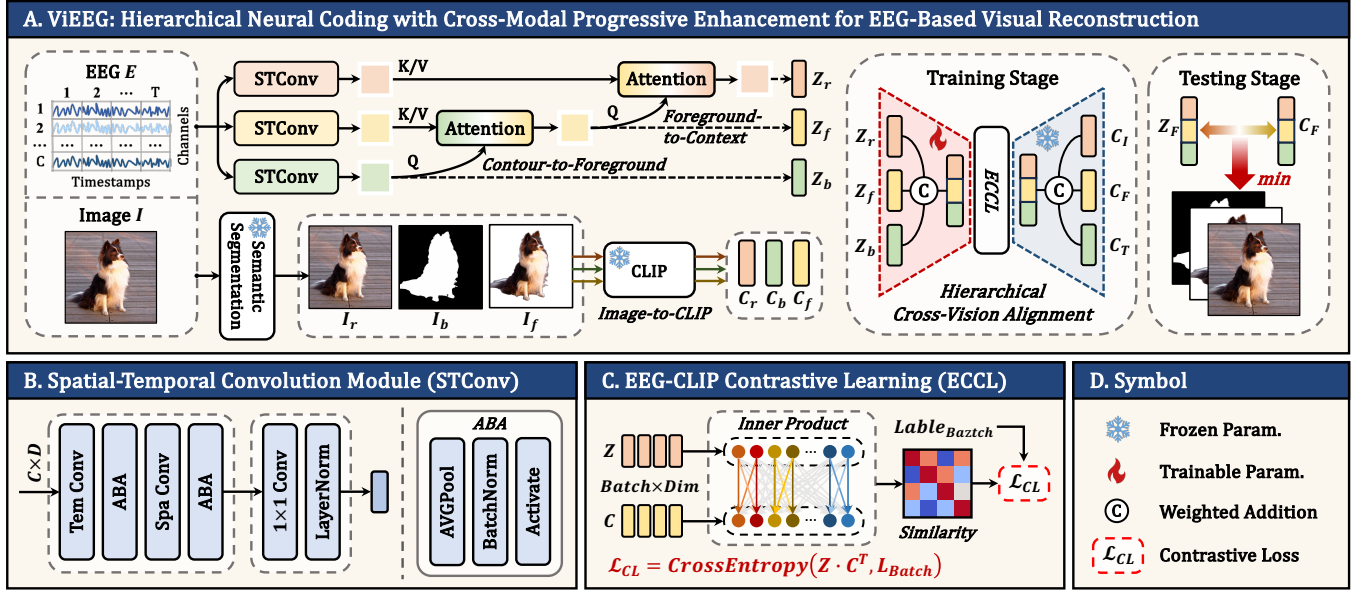


**Figure 3: Overview of the ViEEG framework.** The input image is decomposed into three biologically inspired views: binary mask, foreground object, and raw scene. Corresponding EEG responses are encoded by parallel spatiotemporal encoders, integrated via hierarchical cross-attention, and aligned with CLIP embeddings through hierarchical contrastive learning.

attention weights. The final feature for each head is computed as:

$$F^i = \text{Attention}(Q^i, K^i, V^i) = \text{softmax} \left( \frac{Q^i K^i T}{\sqrt{d}} \right) V^i \quad (7)$$

where  $d$  is the normalization hyperparameter. The output of the multi-head self-attention is then given by:

$$F = \text{MHA}(K = a, Q = V = b) = (F^1 \| F^2 \| \dots \| F^h) W^O + b \quad (8)$$

where  $\text{MHA}(\cdot)$  denote multi-head attention function,  $h$  is the number of attention heads,  $W^O$  is a linear transformation, and  $\|$  denotes concatenation.

**Contour-to-object Integration:** The low-level representation is the contour feature  $F_b^{init}$ , while the high-level representation is the object feature  $F_f^{init}$ . The refined object feature is computed as:

$$F_f = \text{LN} \left( F_f^{init} + \text{Dropout} \left( \text{MHA}(K = F_b^{init}, Q = V = F_f^{init}) \right) \right) \quad (9)$$

**Object-to-context Integration:** The low-level representation is the object feature  $F_f^{init}$ , while the high-level representation is the context feature  $F_r^{init}$ . The refined context feature is computed as:

$$F_r = \text{LN} \left( F_r^{init} + \text{Dropout} \left( \text{MHA}(K = F_f, Q = V = F_r^{init}) \right) \right) \quad (10)$$

## 4.6 Hierarchical Contrastive Learning

To further enhance representation learning, we adopt a contrastive learning framework that aligns the concatenated EEG features with their corresponding image embeddings. Specifically, we first concatenate the hierarchical EEG features, i.e.,  $F_{\text{eeg}} = (F_b \| F_f \| F_r)$ , and similarly, the image features are concatenated as  $C_{\text{img}} = (C_b \| C_f \| C_r)$ . We then compute the cosine similarity between these concatenated features, scaled by a learnable temperature parameter  $\alpha$

(with  $\alpha = \exp(\text{logit\_scale})$ ). The final loss is computed as the cross-entropy loss on the resulting similarity logits:

$$\mathcal{L} = \text{CrossEntropy} \left( \alpha \cdot \cos(F_{\text{eeg}}, C_{\text{img}}), Y \right) \quad (11)$$

where  $\cos(\cdot, \cdot)$  is cosine similarity function, and  $Y$  denotes the ground-truth labels. This formulation encourages the EEG features to closely align with the corresponding image features in the shared embedding space.

## 5 Experiment

### 5.1 Dataset

The THINGS-EEG dataset [11] is a large-scale benchmark for zero-shot EEG-based object recognition, comprising brain responses from ten participants exposed to images from the THINGS database under a rapid serial visual presentation (RSVP) [34] paradigm. Each stimulus was displayed for 100 ms, followed by a 100 ms inter-stimulus interval (ISI) with a blank screen. The dataset comprises 1654 training concepts and 200 zero-shot test concepts, yielding a total of 82,160 trials per subject. EEG signals were acquired using a 64-channel cap, band-pass filtered between 0.1–100 Hz, and subsequently downsampled to 100 Hz. Preprocessing involved segmenting epochs from 200 ms before to 800 ms after stimulus onset, followed by baseline correction using the pre-stimulus interval.

### 5.2 Experimental Details

All experiments were implemented in PyTorch and conducted on an NVIDIA RTX 3090 (4-GPU) environment. The key hyperparameters include a mask threshold  $\tau = 0.5$ , temporal convolution kernel size  $1 \times 25$ , spatial convolution kernel  $63 \times 1$ , average pooling kernels  $1 \times 51$  and  $1 \times 5$ , a dropout rate of 0.5, attention layer depth of 1,

Method	Subject 1		Subject 2		Subject 3		Subject 4		Subject 5		Subject 6		Subject 7		Subject 8		Subject 9		Subject 10		Ave	
	top-1	top-5	top-1																			
Subject dependent - train and test on one subject																						
BraVL [8]	6.1	17.9	4.9	14.9	5.6	17.4	5.0	15.1	4.0	13.4	6.0	18.2	6.5	20.4	8.8	23.7	4.3	14.0	7.0	19.7	5.8	17.5
LSTM [14]	16.4	43.5	16.1	40.2	20.7	49.4	18.6	42.3	14.2	35.2	18.2	43.1	18.7	47.2	22.0	47.9	16.8	43.8	21.7	52.2	18.3	44.5
ConvNet [27]	14.9	39.3	18.9	42.1	17.8	49.0	23.9	55.8	12.2	32.9	20.1	46.5	15.5	42.6	20.7	48.9	20.7	49.8	19.3	47.5	18.4	45.5
Conformer [32]	11.4	32.4	15.2	41.9	19.8	50.9	23.0	56.6	13.6	33.4	18.1	49.0	18.5	48.2	27.1	56.9	15.2	40.0	22.6	57.8	18.5	46.7
DGCNN [30]	12.3	36.6	11.5	39.5	15.7	43.8	19.7	50.6	10.6	32.6	15.4	46.6	14.0	43.2	25.1	54.5	16.0	43.7	17.9	53.0	15.8	44.4
EEGNet [17]	16.0	42.9	17.9	48.6	18.2	51.5	23.9	59.0	14.4	37.7	19.5	52.0	18.5	50.2	30.2	61.2	23.3	51.2	22.5	58.3	20.4	51.2
Mb2C [36]	23.6	56.3	22.6	50.5	26.3	60.1	34.8	67.0	21.3	53.0	31.0	62.3	25.0	54.8	39.0	69.3	27.5	59.3	33.1	70.8	28.4	60.3
NICE [31]	21.7	51.2	23.3	55.0	29.1	60.5	32.3	69.6	18.2	45.6	29.3	62.1	24.3	59.2	41.3	72.4	24.3	59.0	28.9	62.6	27.3	59.7
ATM [20]	25.6	60.5	22.0	54.5	25.0	62.4	31.4	60.9	12.9	43.0	21.3	51.1	30.5	61.5	38.8	72.0	24.4	51.5	29.1	63.5	26.1	58.1
CogCap [40]	27.2	59.5	28.7	56.9	37.1	66.1	37.6	63.2	21.8	47.7	31.5	58.0	32.8	59.5	47.6	73.5	33.3	57.6	35.0	63.5	33.3	60.5
<b>ViEEG</b>	<b>34.1</b>	<b>71.3</b>	<b>38.4</b>	<b>67.9</b>	<b>40.6</b>	<b>74.7</b>	<b>50.1</b>	<b>80.8</b>	<b>28.9</b>	<b>61.5</b>	<b>44.3</b>	<b>76.5</b>	<b>38.6</b>	<b>75.2</b>	<b>54.0</b>	<b>82.5</b>	<b>37.3</b>	<b>74.9</b>	<b>42.8</b>	<b>79.8</b>	<b>40.9</b>	<b>74.5</b>
Subject independent - leave one subject out for test																						
BraVL [8]	2.3	8.0	1.5	6.3	1.4	5.9	1.7	6.7	1.5	5.6	1.8	7.2	2.1	8.1	2.2	7.6	1.6	6.4	2.3	8.5	1.8	7.0
LSTM [14]	9.2	30.3	10.3	26.4	6.4	19.3	9.1	25.2	7.8	22.2	8.4	27.6	7.5	22.0	10.6	26.9	5.3	22.6	9.3	26.1	8.4	24.8
ConvNet [27]	10.4	31.5	14.2	35.0	8.7	26.9	12.1	31.4	5.7	22.5	10.2	28.0	8.3	22.5	10.0	29.9	6.6	19.8	12.2	34.0	9.8	28.2
Conformer [32]	6.3	22.3	5.7	20.4	5.8	15.7	7.8	21.8	6.7	18.4	10.4	32.9	7.0	24.1	9.1	25.2	5.0	17.2	11.7	33.2	7.5	23.1
DGCNN [30]	10.8	30.6	11.9	31.3	6.3	21.3	8.2	24.6	6.1	18.5	11.2	30.4	6.8	20.5	11.0	28.6	9.4	25.4	12.2	30.6	9.4	26.2
EEGNet [17]	11.0	31.1	11.4	34.0	6.5	24.7	13.4	34.4	6.7	26.7	8.5	29.4	7.9	22.0	10.7	32.9	8.9	27.7	15.1	41.6	10.0	30.4
Mb2C [36]	10.5	28.1	11.3	32.8	8.8	27.6	13.6	33.5	10.6	27.5	12.1	33.1	11.5	31.8	12.0	32.1	12.1	31.3	16.1	42.1	11.9	32.0
NICE [31]	13.5	39.3	16.7	42.7	12.4	35.5	17.9	41.9	14.7	38.1	15.6	44.6	13.6	39.0	13.5	37.2	17.0	42.0	22.8	50.7	15.7	41.1
ATM [20]	17.1	41.8	20.2	44.2	13.2	36.7	17.0	40.7	15.1	41.0	13.5	38.3	10.1	29.0	15.2	41.9	13.5	38.4	20.0	45.4	15.5	39.6
CogCap [40]	16.3	42.3	16.2	37.9	8.8	26.8	15.4	37.6	10.1	31.7	14.0	35.4	10.7	26.9	13.9	34.2	9.0	32.4	15.3	38.6	13.0	34.4
<b>ViEEG</b>	<b>22.7</b>	<b>53.5</b>	<b>24.7</b>	<b>52.5</b>	<b>19.0</b>	<b>48.4</b>	<b>25.5</b>	<b>54.1</b>	<b>19.8</b>	<b>47.3</b>	<b>20.7</b>	<b>49.3</b>	<b>20.9</b>	<b>49.4</b>	<b>20.8</b>	<b>46.8</b>	<b>23.8</b>	<b>52.7</b>	<b>31.2</b>	<b>60.3</b>	<b>22.9</b>	<b>51.4</b>

Table 2: Overall accuracy (%) comparison: Top-1 and Top-5 in 200-way zero-shot object recognition

Method	Subject 1		Subject 2		Subject 3		Subject 4		Subject 5		Subject 6		Subject 7		Subject 8		Subject 9		Subject 10		Ave	
	top-1	top-5	top-1																			
Subject dependent - train and test on one subject																						
<i>F<sub>b</sub></i> -Only	14.2	41.8	14.0	39.8	17.0	39.1	20.9	53.2	8.6	30.3	13.6	40.9	14.7	40.7	17.6	46.4	12.8	37.6	14.8	44.0	14.8	41.4
<i>F<sub>f</sub></i> -Only	22.2	52.1	24.5	56.1	29.9	66.0	34.0	67.1	19.2	50.0	32.5	63.5	26.5	58.7	38.7	73.9	29.3	61.8	31.8	68.5	28.9	61.8
<i>F<sub>r</sub></i> -Only	22.1	52.6	24.8	58.0	32.4	62.7	33.1	67.4	18.5	49.1	29.7	66.2	26.8	60.1	40.6	74.1	27.4	62.5	31.8	68.6	28.6	62.1
w/o C-Att	32.4	66.8	34.6	65.9	39.1	71.3	46.5	80.2	27.2	59.8	40.5	74.3	35.3	71.3	52.2	80.8	34.6	71.9	43.9	75.5	38.6	71.8
<b>ViEEG</b>	<b>34.1</b>	<b>71.3</b>	<b>38.4</b>	<b>67.9</b>	<b>40.6</b>	<b>74.7</b>	<b>50.1</b>	<b>80.8</b>	<b>28.9</b>	<b>61.5</b>	<b>44.3</b>	<b>76.5</b>	<b>38.6</b>	<b>75.2</b>	<b>54.0</b>	<b>82.5</b>	<b>37.3</b>	<b>74.9</b>	<b>42.8</b>	<b>79.8</b>	<b>40.9</b>	<b>74.5</b>
Subject independent - leave one subject out for test																						
<i>F<sub>b</sub></i> -Only	5.9	18.6	7.9	22.7	5.7	19.1	7.4	26.3	7.6	20.5	4.2	18.6	9.0	23.1	7.9	21.8	7.0	20.8	10.2	30.9	7.3	22.3
<i>F<sub>f</sub></i> -Only	15.8	43.0	19.8	42.5	13.3	40.3	20.5	45.1	13.7	37.1	17.1	41.7	13.2	39.7	15.5	41.9	15.3	42.9	23.4	51.4	16.8	42.6
<i>F<sub>r</sub></i> -Only	14.9	41.5	18.4	45.9	14.1	41.3	18.1	42.2	15.9	38.3	18.5	42.8	15.4	41.5	16.0	41.6	18.3	45.3	20.5	50.2	17.0	43.1
w/o C-Att	19.1	52.1	22.0	48.9	15.1	45.1	24.2	55.2	16.7	41.6	21.0	50.4	17.2	44.7	19.5	45.6	20.9	48.8	31.1	59.8	20.7	49.2
<b>ViEEG</b>	<b>22.7</b>	<b>53.5</b>	<b>24.7</b>	<b>52.5</b>	<b>19.0</b>	<b>48.4</b>	<b>25.5</b>	<b>54.1</b>	<b>19.8</b>	<b>47.3</b>	<b>20.7</b>	<b>49.3</b>	<b>20.9</b>	<b>49.4</b>	<b>20.8</b>	<b>46.8</b>	<b>23.8</b>	<b>52.7</b>	<b>31.2</b>	<b>60.3</b>	<b>22.9</b>	<b>51.4</b>

Table 3: Ablation study: Top-1 and Top-5 accuracy (%) in 200-way zero-shot object recognition

and 3 attention heads. The model is optimized using Adam with a batch size of 1000 and a learning rate of  $2 \times 10^{-3}$ .

For fair comparison, experiments were conducted under subject-dependent and subject-independent settings, following the protocol of ATM [20]. All methods used the same CLIP backbone (CLIP-ViT-H/14<sup>7</sup>) to ensure alignment consistency. For subject-dependent training, 740 trials were randomly selected as the validation set, and the model with the lowest validation loss was retained. In the subject-independent setting, we employed a leave-one-subject-out (LOSO) protocol, using 6660 trials for validation in each fold. All experiments were repeated five times, and the average test accuracy was reported to mitigate variance and ensure result robustness.

<sup>7</sup><https://huggingface.co/laion/CLIP-ViT-bigG-14-laion2B-39B-b160k>

### 5.3 Overall Performance

The experimental comparison against state-of-the-art methods demonstrates ViEEG's superior decoding capability across both evaluation paradigms. We conduct comprehensive comparisons against 10 EEG decoding methods, including BraVL [8], LSTM [14], ConvNet [27], Conformer [32], DGCNN [30], EEGNet [17], MB2C [36], NICE [31], ATM [20], and CognitionCapture (CogCap) [40]. Table 2 summarizes the 200-way zero-shot recognition performance across

Metric	ViEEG	NICE	Improve	Best Case (Sub.10)
Avg. Top-1 (Dep.)	40.9%	27.3%	49.82%	42.8% vs 28.9% (↑ 48.1%)
Avg. Top-5 (Dep.)	74.5%	59.7%	24.79%	79.8% vs 62.6% (↑ 27.5%)
Avg. Top-1 (Ind.)	22.9%	15.7%	45.86%	31.2% vs 22.8% (↑ 36.8%)
Avg. Top-5 (Ind.)	51.4%	41.1%	25.06%	60.3% vs 50.7% (↑ 19.0%)

Table 4: Summary of recognition performance and relative improvement over NICE across Top-1 and Top-5 metrics.

both experimental paradigms, and our method ViEEG achieves consistent improvements over existing approaches through biologically grounded hierarchical modeling.

**Subject-dependent Experiments:** ViEEG achieves new performance benchmarks, reaching **40.9%** Top-1 and **74.5%** Top-5 average accuracy across 10 subjects, outperforming the previous SOTA method by substantial margins. Specifically, compared to the baseline NICE, ViEEG demonstrates an average improvement of **49.82%** in Top-1 accuracy and **24.79%** in Top-5 accuracy, reflecting its capacity to effectively exploit subject-specific neural patterns. This performance highlights its enhanced capacity of ViEEG to handle visual scenes through hierarchical feature disentanglement.

**Cross-subject Experiments:** When tested on unseen subjects under LOSO protocol, ViEEG maintains robust performance with **22.9%** Top-1 and **51.4%** Top-5 accuracy. The biological plausibility of our hierarchical design enables better generalization compared to NICE's flat representation approach. For average object recognition accuracy, ViEEG demonstrates relative improvement of **45.86%** in Top-1 accuracy and **25.06%** in Top-5 accuracy. This performance gap stems from ViEEG's hierarchical feature disentanglement that captures invariant neural patterns across individuals.

Consistent performance gains across all evaluation metrics (Table 4) statistically validate that explicit modeling of visual processing hierarchy substantially improves EEG decoding accuracy.

## 5.4 ablation Study

We conducted a series of ablation studies to assess the individual contributions of each core module in ViEEG, as summarized in Table 3. More detailed results are provided in the Appendix.

**5.4.1 ablation on Hierarchical Embedding.** This experiment analyzes the effectiveness of different levels of hierarchical EEG embeddings in supporting object recognition. Specifically, we evaluated configurations that utilized only one type of embedding at a time:  $F_b$  (contour-level),  $F_f$  (object-level), and  $F_r$  (scene-level). In the subject-dependent setting,  $F_b$  achieved 14.2% Top-1 and 41.8% Top-5 accuracy. In contrast,  $F_f$  and  $F_r$  both improved performance to approximately 22% Top-1 accuracy. These results suggest that while each representation captures distinct neural cues, none is sufficient alone to support optimal decoding performance. Notably,  $F_f$  and  $F_r$  embeddings, which encode mid- and high-level visual semantics, outperformed  $F_b$ , highlighting the greater salience of semantic and contextual cues in EEG decoding.

**5.4.2 ablation on Cross Attention.** We further examined the role of the cross-attention mechanism in integrating multi-level EEG features across the visual hierarchy. Ablating the cross-attention module (denoted as w/o C-Att) led to noticeable performance degradation across all settings. For instance, in the subject-dependent setting, the Top-1 and Top-5 accuracies dropped from 34.1% and 71.3% to 32.4% and 66.8%, respectively, when cross-attention was removed. In the subject-independent setting, similar trends were observed, with the full ViEEG model outperforming the variant without cross-attention by notable margins. These findings underscore the importance of cross-attention for aligning and integrating hierarchical EEG embeddings, thereby enhancing overall model robustness and generalization across subjects. The performance gain

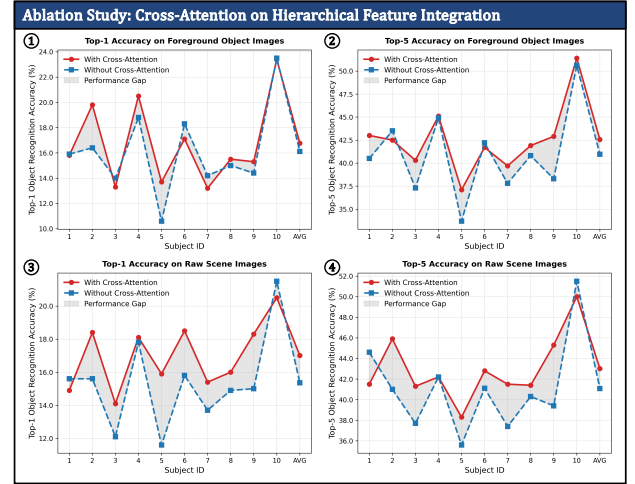


**Figure 4: Impact of Cross-Attention on Feature Integration.** Subfigures 1 and 2 show the Top-1 and Top-5 accuracies of foreground object embedding ( $F_f$ ) with and without cross-attention, and subfigures 3 and 4 report the same metrics for scene embedding ( $F_r$ ).

is particularly evident in the integration of  $F_f$  and  $F_r$ , as visualized in Figure 4, where the majority of subjects demonstrate that adding cross-attention for hierarchical visual information integration effectively improves EEG decoding of the integrated features.

## 6 Discussion

### 6.1 Representational Analysis

To assess the representational consistency of ViEEG, we visualize the Representational Similarity Matrix (RSM) in the form of heatmaps, using data from Subject 8 of the THINGS-EEG dataset. The RSM quantifies pairwise similarity among neural representations across different visual categories, offering insight into how well the learned embeddings preserve intrinsic EEG structure. For comparison, we also visualize the corresponding RSMs generated by NICE and ATM, as shown in Figure 5. More results from other subjects are provided in the Appendix.

The RSMs of all three methods exhibit block-diagonal patterns when test samples are ordered by category, indicating basic inter-class separability. However, ViEEG distinguishes itself by preserving sharper main diagonals within each block, reflecting stronger intra-class consistency and more precise instance-level matching. For example, in the "Food" category, ViEEG consistently localizes target representations with clear diagonal peaks, while NICE and ATM produce more diffuse patterns with less focus on the diagonal. This suggests that ViEEG can better discriminate among similar samples within a class. In contrast, ambiguous categories like "Tool" and "Sports" naturally show less defined separability, and the "Other" class presents no clear structure due to its heterogeneous nature. This dual preservation of class-level structure and instance-level discrimination highlights ViEEG's potential in real-world EEG retrieval and classification tasks, where both categorical understanding and exemplar precision are essential.

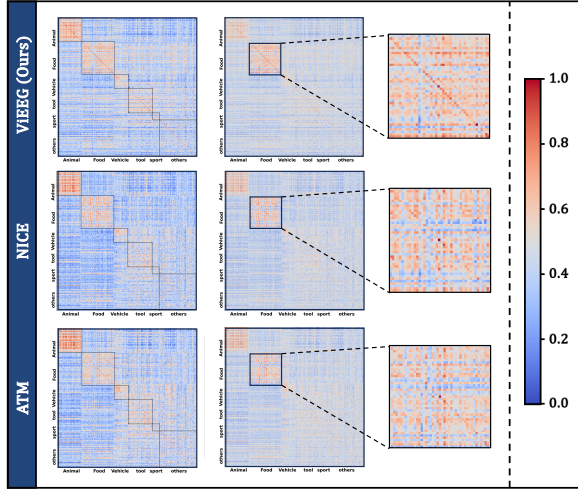


**Figure 5: Representative Similarity Matrices of ViEEG, NICE, and ATM.** Top row: RSMs across six major categories (Animal, Food, Vehicle, Tool, Sports, and Other). Bottom row: Zoomed-in view of the Food category.

## 6.2 Brain Decoding Results Analysis

**6.2.1 Zero-shot Image Retrieval.** To further evaluate ViEEG’s capacity for visual concept decoding from EEG, we conduct zero-shot image retrieval experiments based on different visual embeddings: binary object mask (BOM), foreground object (FO), and raw scene (RS) embedding, as well as concatenated triple visual embedding. As shown in Figure 6, each embedding variant demonstrates distinct advantages depending on the object’s visual structure and contextual complexity. For example, for the basketball, BOM yields the highest retrieval accuracy, likely due to the clean, circular silhouette of the ball. In contrast, FO and RS embeddings underperform, possibly due to background clutter or inconsistent attentional focus during EEG acquisition. Conversely, for the aircraft carrier, the complex object geometry and blended ocean background reduce BOM and RS effectiveness, making FO the most discriminative embedding.

Crucially, concatenating all three embeddings—forming the Tri-View representation—consistently yields superior performance. This suggests a complementary mechanism, where confident predictions from any individual view elevate the joint similarity score, mitigating retrieval errors caused by weaker modalities. Additional retrieval results are provided in the Appendix to further demonstrate the robustness and reliability of our framework.

**6.2.2 Image Reconstruction.** To further assess the visual fidelity of ViEEG’s learned representations, we perform image reconstruction using visual embeddings derived from EEG. As shown in Figure 1, the reconstructed images preserve key semantic information of the original stimuli, including object category, shape, and spatial structure. Notably, ViEEG is capable of reconstructing both the foreground object and its contour, demonstrating its capacity to capture fine-grained visual features from brain signals. Due to space limitations, more reconstruction examples and implementation details are provided in the Appendix.

## 6.3 Parameter Analysis

ViEEG integrates a cross-attention module to hierarchically fuse contour, object, and context-level EEG features. We perform grid search experiments to explore the impact of attention layers and heads under both subject-dependent and subject-independent settings (Figure 7). Varying the number of attention layers from 0 to 5, we find that a single-layer configuration yields the best Top-1 accuracy in both settings. Deeper attention stacks lead to overfitting or marginal gains, making one layer the optimal balance between performance and complexity. For attention heads, we test 1 to 6 heads. Three heads achieve the highest accuracy in the subject-dependent case, while subject-independent performance remains relatively stable across configurations. Overall, ViEEG performs best with one attention layer and three heads.

## 7 Conclusion

In this work, we proposed ViEEG, a novel EEG-based visual decoding framework that emulates the hierarchical structure of human visual perception. By integrating biologically motivated image decomposition with hierarchical EEG encoding and cross-attention fusion, ViEEG captures the progressive flow of visual information from edge detection to semantic and contextual understanding. This design directly addresses the critical issue of hierarchical neural encoded neglect (HNEN) in conventional EEG decoding approaches. Through extensive experiments on the THINGS-EEG dataset, ViEEG significantly outperformed state-of-the-art baselines in both subject-dependent and cross-subject zero-shot recognition tasks. Ablation studies further validate the importance of each component, particularly the hierarchical embedding structure and cross-attention integration. Beyond performance gains, ViEEG offers a cognitively plausible model that strengthens the connection between neuroscience and artificial intelligence. We believe this work opens up new possibilities for neuro-inspired learning and brings us closer to more accurate, interpretable, and generalizable brain-computer interface systems.

## References

- [1] Emily J Allen, Ghislain St-Yves, Yihan Wu, Jesse L Breedlove, Jacob S Prince, Logan T Dowdle, Matthias Nau, Brad Caron, Franco Pestilli, Ian Charest, et al. 2022. A massive 7T fMRI dataset to bridge cognitive neuroscience and artificial intelligence. *Nature Neuroscience* 25, 1 (2022), 116–126.
- [2] Michael J Arcaro and Margaret S Livingstone. 2021. On the relationship between maps and domains in inferotemporal cortex. *Nature Reviews Neuroscience* 22, 9 (2021), 573–583.
- [3] Yinpeng Bai, Xintao Wang, Yan-pei Cao, Yixiao Ge, Chun Yuan, and Ying Shan. 2023. Dreamdiffusion: Generating high-quality images from brain eeg signals. *arXiv preprint arXiv:2306.16934* (2023).
- [4] Rami Ben-Yishai, R Lev Bar-Or, and Haim Sompolinsky. 1995. Theory of orientation tuning in visual cortex. *Proceedings of the National Academy of Sciences* 92, 9 (1995), 3844–3848.
- [5] Holly Bridge, Stuart Clare, Mark Jenkinson, Peter Jezzard, Andrew J Parker, and Paul M Matthews. 2005. Independent anatomical and functional measures of the V1/V2 boundary in human visual cortex. *Journal of Vision* 5, 2 (2005), 1–1.
- [6] Xupeng Chen, Ran Wang, Amirhossein Khalilian-Gourtani, Leyao Yu, Patricia Dugan, Daniel Friedman, Werner Doyle, Orrin Devinsky, Yao Wang, and Adeen Flinker. 2024. A neural speech decoding framework leveraging deep learning and speech synthesis. *Nature Machine Intelligence* 6, 4 (2024), 467–480.
- [7] Alexander Craik, Yongtian He, and Jose L Contreras-Vidal. 2019. Deep learning for electroencephalogram (EEG) classification tasks: a review. *Journal of Neural Engineering* 16, 3 (2019), 031001.
- [8] Changde Du, Kaicheng Fu, Jinpeng Li, and Huiguang He. 2023. Decoding visual neural representations by multimodal learning of brain-visual-linguistic features.

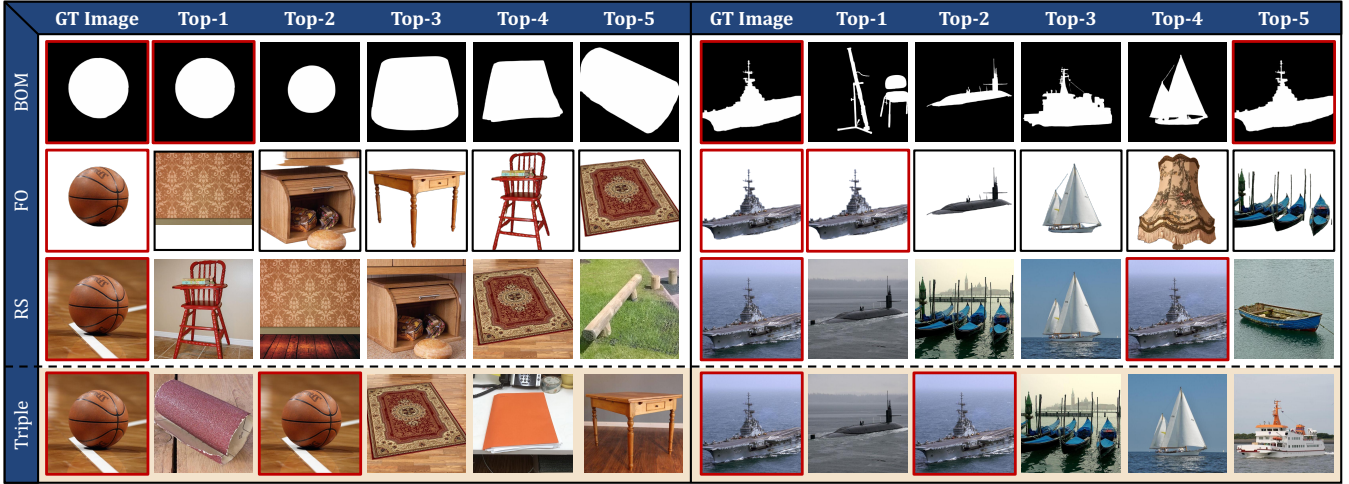


**Figure 6: Zero-shot Image Retrieval with Different Embeddings (Subject 8).** Left: Basketball example shows BOM excels due to clean contours. Right: Aircraft carrier case favors FO due to complex shape and background blending.

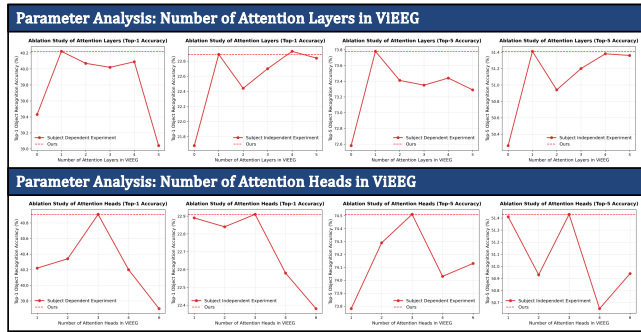


**Figure 7: Parameter Analysis for the Attention Module.** Top row: Accuracy trends for varying numbers of attention layers; Bottom row: Accuracy trends for different numbers of attention heads. Both Top-1 and Top-5 metrics under subject-dependent and subject-independent settings are reported.

*IEEE Transactions on Pattern Analysis and Machine Intelligence* 45, 9 (2023), 10760–10777.

- [9] Daniel J Felleman and David C Van Essen. 1991. Distributed hierarchical processing in the primate cerebral cortex. *Cerebral cortex (New York, NY: 1991)* 1, 1 (1991), 1–47.
- [10] Honghao Fu, Hao Wang, Jing Jih Chin, and Zhiqi Shen. 2025. BrainVis: Exploring the bridge between brain and visual signals via image reconstruction. In *ICASSP 2025–2025 IEEE International Conference on Acoustics, Speech and Signal Processing (ICASSP)*. IEEE, 1–5.
- [11] Alessandro T Gifford, Kshitij Dwivedi, Gemma Roig, and Radoslaw M Cichy. 2022. A large and rich EEG dataset for modeling human visual object recognition. *NeuroImage* 264 (2022), 119754.
- [12] Kalanit Grill-Spector and Rafael Malach. 2004. The human visual cortex. *Annu. Rev. Neurosci.* 27, 1 (2004), 649–677.
- [13] Kathleen A Hansen, Kendrick N Kay, and Jack L Gallant. 2007. Topographic organization in and near human visual area V4. *Journal of Neuroscience* 27, 44 (2007), 11896–11911.
- [14] S Hochreiter. 1997. Long Short-term Memory. *Neural Computation MIT-Press* (1997).
- [15] Tomoyasu Horikawa and Yukiyasu Kamitani. 2017. Generic decoding of seen and imagined objects using hierarchical visual features. *Nature Communications* 8, 1 (2017), 15037.
- [16] Jingyang Huo, Yikai Wang, Yun Wang, Xuelin Qian, Chong Li, Yanwei Fu, and Jianfeng Feng. 2024. Neuropictor: Refining fmri-to-image reconstruction via multi-individual pretraining and multi-level modulation. In *European Conference*

on Computer Vision. Springer, 56–73.

- [17] Vernon J Lawhern, Amelia J Solon, Nicholas R Waytowich, Stephen M Gordon, Chou P Hung, and Brent J Lance. 2018. EEGNet: a compact convolutional neural network for EEG-based brain–computer interfaces. *Journal of Neural Engineering* 15, 5 (2018), 056013.
- [18] Seo-Hyun Lee, Minji Lee, and Seong-Whan Lee. 2020. Neural decoding of imagined speech and visual imagery as intuitive paradigms for BCI communication. *IEEE Transactions on Neural Systems and Rehabilitation Engineering* 28, 12 (2020), 2647–2659.
- [19] Bin Li, Yuki Todo, and Zheng Tang. 2022. Artificial visual system for orientation detection based on Hubel–Wiesel model. *Brain Sciences* 12, 4 (2022), 470.
- [20] Dongyang Li, Chen Wei, Shiyi Li, Jiachen Zou, Haoyang Qin, and Quanying Liu. 2024. Visual decoding and reconstruction via eeg embeddings with guided diffusion. *The Thirty-eighth Annual Conference on Neural Information Processing Systems (2024)*.
- [21] Xuan-Hao Liu, Yan-Kai Liu, Yansen Wang, Kan Ren, Hanwen Shi, Zilong Wang, Dongsheng Li, Bao-Liang Lu, and Wei-Long Zheng. 2024. EEG2Video: Towards decoding dynamic visual perception from EEG signals. *Advances in Neural Information Processing Systems* 37 (2024), 72245–72273.
- [22] Dustin Podell, Zion English, Kyle Lacey, Andreas Blattmann, Tim Dockhorn, Jonas Müller, Joe Penna, and Robin Rombach. 2023. Sdxl: Improving latent diffusion models for high-resolution image synthesis. *arXiv preprint arXiv:2307.01952* (2023).
- [23] Alec Radford, Jong Wook Kim, Chris Hallacy, Aditya Ramesh, Gabriel Goh, Sandhini Agarwal, Girish Sastry, Amanda Askell, Pamela Mishkin, Jack Clark, et al. 2021. Learning transferable visual models from natural language supervision. In *International conference on machine learning*. PMLR, 8748–8763.
- [24] Zarina Rakhiberdina, Quentin Jodelet, Xin Liu, and Tsuyoshi Murata. 2021. Natural image reconstruction from fmri using deep learning: A survey. *Frontiers in Neuroscience* 15 (2021), 795488.
- [25] Aditya Ramesh, Prafulla Dharwal, Alex Nichol, Casey Chu, and Mark Chen. 2022. Hierarchical text-conditional image generation with clip latents. *arXiv preprint arXiv:2204.06125* 1, 2 (2022), 3.
- [26] Maximilian Riesenhuber and Tomaso Poggio. 1999. Hierarchical models of object recognition in cortex. *Nature Neuroscience* 2, 11 (1999), 1019–1025.
- [27] Robin Tibor Schirrmeister, Jost Tobias Springenberg, Lukas Dominique Josef Fiederer, Martin Glasstetter, Katharina Eggensperger, Michael Tangermann, Frank Hutter, Wolfram Burgard, and Tonio Ball. 2017. Deep learning with convolutional neural networks for EEG decoding and visualization. *Human Brain Mapping* 38, 11 (2017), 5391–5420.
- [28] Paul Scotti, Atmadeep Banerjee, Jimmie Goode, Stepan Shabalin, Alex Nguyen, Aidan Dempster, Nathalie Verlinde, Elad Yundler, David Weisberg, Kenneth Norman, et al. 2023. Reconstructing the mind’s eye: fmri-to-image with contrastive learning and diffusion priors. *Advances in Neural Information Processing Systems* 36 (2023), 24705–24728.
- [29] Nanlin Shi, Yining Miao, Changxing Huang, Xiang Li, Yonghao Song, Xiaogang Chen, Yijun Wang, and Xiaorong Gao. 2024. Estimating and approaching the maximum information rate of noninvasive visual brain-computer interface. *NeuroImage* 289 (2024), 120548.

- [30] Tengfei Song, Wenming Zheng, Peng Song, and Zhen Cui. 2018. EEG emotion recognition using dynamical graph convolutional neural networks. *IEEE Transactions on Affective Computing* 11, 3 (2018), 532–541.
- [31] Yonghao Song, Bingchuan Liu, Xiang Li, Nanlin Shi, Yijun Wang, and Xiaorong Gao. 2024. Decoding Natural Images from EEG for Object Recognition. In *International Conference on Learning Representations*.
- [32] Yonghao Song, Qingqing Zheng, Bingchuan Liu, and Xiaorong Gao. 2022. EEG conformer: Convolutional transformer for EEG decoding and visualization. *IEEE Transactions on Neural Systems and Rehabilitation Engineering* 31 (2022), 710–719.
- [33] Jingyuan Sun, Mingxiao Li, Zijiao Chen, Yunhao Zhang, Shaonan Wang, and Marie-Francine Moens. 2023. Contrast, attend and diffuse to decode high-resolution images from brain activities. *Advances in Neural Information Processing Systems* 36 (2023), 12332–12348.
- [34] Simon Thorpe, Denis Fize, and Catherine Marlot. 1996. Speed of processing in the human visual system. *Nature* 381, 6582 (1996), 520–522.
- [35] Shizun Wang, Songhua Liu, Zhenxiong Tan, and Xinchao Wang. 2024. Mind-bridge: A cross-subject brain decoding framework. In *Proceedings of the IEEE/CVF Conference on Computer Vision and Pattern Recognition*. 11333–11342.
- [36] Yayun Wei, Lei Cao, Hao Li, and Yilin Dong. 2024. MB2C: Multimodal Bidirectional Cycle Consistency for Learning Robust Visual Neural Representations. In *Proceedings of the 32nd ACM International Conference on Multimedia*. 8992–9000.
- [37] Keith J Worsley, Chien Heng Liao, John Aston, V Petre, GH Duncan, F Morales, and Alan C Evans. 2002. A general statistical analysis for fMRI data. *Neuroimage* 15, 1 (2002), 1–15.
- [38] Hu Ye, Jun Zhang, Sibo Liu, Xiao Han, and Wei Yang. 2023. Ip-adapter: Text compatible image prompt adapter for text-to-image diffusion models. *arXiv preprint arXiv:2308.06721* (2023).
- [39] Raheel Zafar, Aamir Saeed Malik, Nidal Kamel, Sarat C Dass, Jafri M Abdullah, Faruque Reza, and Ahmad Helmy Abdul Karim. 2015. Decoding of visual information from human brain activity: A review of fMRI and EEG studies. *Journal of Integrative Neuroscience* 14, 02 (2015), 155–168.
- [40] Kaifan Zhang, Lihuo He, Xin Jiang, Wen Lu, Di Wang, and Ximbo Gao. 2024. CognitionCapturer: Decoding Visual Stimuli From Human EEG Signal With Multimodal Information. *Association for the Advancement of Artificial Intelligence* (2024).
- [41] Qiongyi Zhou, Changde Du, Shengpei Wang, and Huiguang He. 2024. CLIP-MUSED: CLIP-Guided Multi-Subject Visual Neural Information Semantic Decoding. *The Annual Conference on Neural Information Processing Systems* (2024).

## ViEEG: Hierarchical Neural Coding with Cross-Modal Progressive Enhancement for EEG-Based Visual Reconstruction

### Supplementary Material: Appendix

#### A Details of the Datasets

The THINGS-EEG dataset [11], used in this study, is a large-scale EEG dataset designed to model visual object recognition. It includes data from ten participants who were exposed to images from the THINGS database. The images were presented using a rapid serial visual presentation (RSVP) paradigm, where each image was shown for 100 ms followed by a blank screen for 100 ms, maintaining a stimulus onset asynchrony (SOA) of 200 ms. The dataset contains 16,540 training image conditions (1,654 concepts, each with 10 images, repeated four times) and 200 test image conditions (200 concepts, each with one image, repeated once). The THINGS image dataset comprises six major categories, including animals (e.g., cats, dogs), vehicles (e.g., airplanes, ships), food items (e.g., cake, corn), tools (e.g., cameras, phones), sports equipment (e.g., balls, golf clubs), and other miscellaneous categories.

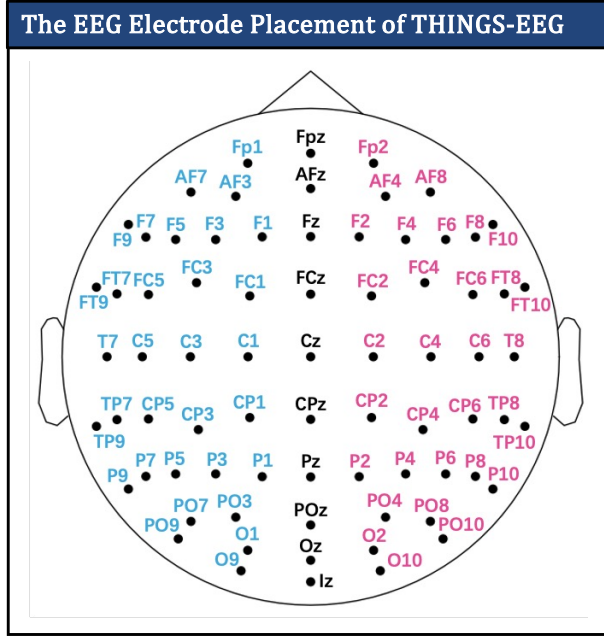


Figure 8: The corresponding EEG 63-electrode placement of THINGS-EEG datasets.

EEG signals were recorded using a 64-channel cap according to the 10-10 system, sampled at 1000 Hz, and filtered within a frequency range of 0.1–100 Hz. Preprocessing included segmenting the data into epochs from 200 ms before to 800 ms after stimulus onset, baseline correction using the mean pre-stimulus interval, and down-sampling to 100 Hz. To reduce noise, repeated trials were averaged, and multivariate noise normalization was applied using training data. For input into the image encoder, images were resized to 224 × 224 pixels and normalized.

#### B Comparison Methods

To validate the efficacy of our proposed approach, we compare ViEEG with a range of classical and recent methods spanning EEG cognitive decoding and visual decoding. Below, we provide detailed descriptions of the competing approaches:

- **BraVL [8]:** BraVL employs multimodal learning to jointly model brain, visual, and linguistic features, maximizing intra- and inter-modality mutual information to improve consistency and data efficiency.
- **LSTM [14]:** Long Short-Term Memory networks are leveraged to capture long-term temporal dependencies in sequential EEG data.
- **ConvNet [27]:** A convolutional neural network designed for end-to-end EEG decoding, focusing on extracting spatial and spectral features directly from raw EEG signals.
- **Conformer [32]:** This architecture combines convolutional neural networks with Transformer modules to extract both local and global dependencies in sequential EEG data.
- **DGCNN [30]:** The Dynamical Graph CNN employs a learnable adjacency matrix along with Chebyshev filters to capture dynamic relationships in EEG data for emotion classification.
- **EEGNet [17]:** A lightweight convolutional network that efficiently extracts temporal and spatial features from EEG signals, optimized for BCI applications.
- **MB2C [36]:** The Multimodal Bidirectional Cycle Consistency framework utilizes dual-GAN architectures to generate and reconcile modality-specific features, effectively bridging the modality gap in zero-shot tasks, EEG classification, and image reconstruction.
- **NICE [31]:** A self-supervised framework that learns image representations from EEG signals by incorporating attention modules to capture spatial correlations within brain activity.
- **ATM [20]:** The Adaptive Thinking Mapper projects neural signals into a shared subspace with CLIP embeddings via a two-stage EEG-to-image generation strategy, enabling zero-shot visual decoding and reconstruction.
- **CognitionCapturer (CogCap) [40]:** This unified framework enhances EEG signal representations by leveraging multimodal data and modality-specific expert encoders. It employs a diffusion prior to map EEG embeddings to the CLIP space, achieving high-fidelity reconstruction of visual stimuli without requiring fine-tuning.

These methods represent a diverse set of strategies for EEG decoding and visual reconstruction, against which ViEEG is rigorously benchmarked.

#### C Whole Results of ablation Study

Due to space limitations, only partial information is presented in the main text. The complete results of the ablation experiments on Hierarchical Embedding and cross-attention are provided here.

$F_b$	$F_f$	$F_r$	Subject-Dependent Setting										Subject-Independent Setting											
			Sub-1	Sub-2	Sub-3	Sub-4	Sub-5	Sub-6	Sub-7	Sub-8	Sub-9	Sub-10	Avg	Sub-1	Sub-2	Sub-3	Sub-4	Sub-5	Sub-6	Sub-7	Sub-8	Sub-9	Sub-10	Avg
Top-1 Accuracy																								
✓	✗	✗	14.2	14.0	17.0	20.9	8.6	13.6	14.7	17.6	12.8	14.8	14.8	5.9	7.9	5.7	7.4	7.6	4.2	9.0	7.9	7.0	10.2	7.28
✗	✓	✗	22.2	24.5	29.9	34.0	19.2	32.5	26.5	38.7	29.3	31.8	28.9	15.8	19.8	13.3	20.5	13.7	17.1	13.2	15.5	15.3	23.4	16.76
✗	✗	✓	22.1	24.8	31.4	33.1	18.5	29.7	26.8	40.6	27.4	31.8	28.6	14.9	18.4	14.1	18.1	15.9	18.5	15.4	16.0	18.3	20.5	17.01
✓	✓	✗	31.4	32.8	35.0	46.4	25.6	37.5	33.3	46.8	33.8	40.3	36.3	16.8	20.4	12.8	20.1	16.1	16.4	17.8	17.6	16.9	28.4	18.33
✓	✗	✓	32.2	30.8	35.6	47.5	24.1	38.1	34.9	45.1	32.0	39.6	36.0	16.5	20.5	13.1	20.6	16.0	18.0	17.6	17.6	19.9	27.5	18.73
✗	✓	✓	25.1	28.8	33.8	39.6	22.0	34.7	28.4	43.0	31.5	33.9	32.1	18.5	21.8	16.7	22.0	19.3	21.3	16.1	18.7	19.8	27.3	20.15
✓	✓	✓	34.1	38.4	40.6	50.1	28.9	44.3	38.6	54.0	37.3	42.8	40.9	22.7	24.7	19.0	25.5	19.8	20.7	20.9	20.8	23.8	31.2	22.91
Top-3 object Recognition Accuracy																								
✓	✗	✗	29.8	30.0	29.8	40.1	20.2	28.6	30.6	35.3	26.7	32.9	30.4	12.7	16.3	13.1	17.6	15.1	12.7	16.9	17.4	15.3	22.6	15.97
✗	✓	✗	41.2	46.0	51.4	58.3	36.6	53.6	45.4	63.3	50.7	58.1	50.5	31.9	34.1	29.4	35.7	28.6	33.6	29.4	32.2	31.5	43.0	32.94
✗	✗	✓	40.6	46.2	51.5	56.8	36.6	55.9	48.9	65.1	51.3	55.9	50.9	32.8	34.2	31.1	29.9	35.7	31.2	32.3	35.8	39.1	33.52	
✓	✓	✗	54.3	53.5	57.6	69.9	45.6	60.8	56.7	69.4	56.7	62.0	58.7	33.2	35.0	30.4	39.4	28.5	32.4	33.3	31.1	32.5	47.6	34.34
✓	✗	✓	56.2	53.4	57.7	68.8	43.5	60.1	57.9	69.7	55.5	63.4	58.6	34.0	38.9	32.7	39.0	31.5	34.1	33.0	32.4	34.2	45.4	35.52
✗	✓	✓	46.5	50.4	56.3	61.2	40.9	57.8	52.3	68.7	56.0	61.1	55.1	35.2	38.5	34.5	38.3	34.4	36.4	33.8	36.6	38.1	46.3	37.21
✓	✓	✓	58.3	58.1	62.6	72.2	52.3	66.8	63.2	74.1	62.0	68.9	63.9	43.1	43.2	36.6	45.4	37.2	37.8	38.8	36.9	41.5	51.0	41.15
Top-5 object Recognition Accuracy																								
✓	✗	✗	41.8	39.8	39.1	53.2	30.3	40.9	40.7	46.4	37.6	44.0	41.4	18.6	22.8	19.1	26.3	20.5	18.6	23.1	21.8	20.8	30.9	22.25
✗	✓	✗	52.1	56.1	66.0	67.1	50.0	63.5	58.7	73.9	61.8	68.5	61.8	43.0	42.5	40.3	45.1	37.1	41.7	39.7	41.9	42.9	51.4	42.56
✗	✗	✓	52.6	58.0	62.7	67.4	49.1	66.2	60.1	74.1	62.5	68.6	62.1	41.5	45.9	41.3	42.2	38.3	42.8	41.5	41.4	45.3	50.0	43.02
✓	✓	✗	64.5	62.7	69.2	78.8	55.5	73.0	69.3	78.1	66.8	72.5	69.0	43.7	45.6	40.2	47.9	38.8	41.3	43.1	39.3	42.8	56.3	43.90
✓	✗	✓	66.4	63.2	69.7	78.3	54.8	72.7	69.5	79.0	65.2	72.6	69.1	43.9	46.8	42.8	49.1	41.0	41.9	42.0	39.6	46.6	54.5	44.82
✗	✓	✓	57.8	62.2	68.3	70.8	52.5	66.9	64.7	77.7	66.9	72.0	66.0	45.1	48.1	46.5	46.7	43.7	45.8	45.0	45.5	49.3	56.7	47.24
✓	✓	✓	71.3	67.9	74.7	80.8	61.5	76.5	75.2	82.5	74.9	79.8	74.5	53.5	52.5	48.4	54.1	47.3	49.3	49.4	46.8	52.7	60.3	51.43

Table 5: Object Recognition Accuracy for Different Hierarchical Feature Combinations in ViEEG with cross-attention module

$F_b$	$F_f$	$F_r$	Subject-Dependent Setting										Subject-Independent Setting											
			Sub-1	Sub-2	Sub-3	Sub-4	Sub-5	Sub-6	Sub-7	Sub-8	Sub-9	Sub-10	Avg	Sub-1	Sub-2	Sub-3	Sub-4	Sub-5	Sub-6	Sub-7	Sub-8	Sub-9	Sub-10	Avg
Top-1 Accuracy																								
✓	✗	✗	15.9	14.5	16.0	20.1	9.7	11.3	15.3	17.9	12.0	15.1	14.8	5.5	8.7	5.8	7.1	6.2	4.7	9.0	8.9	7.3	11.2	7.44
✗	✓	✗	21.4	22.8	28.6	34.6	19.4	26.0	26.8	38.6	21.8	30.8	27.1	15.9	16.4	14.0	18.8	10.6	18.3	14.2	15.0	14.4	23.5	16.11
✗	✗	✓	21.6	23.2	27.8	33.4	18.9	28.1	25.8	35.6	23.4	32.8	27.1	15.6	15.6	12.1	17.8	11.6	15.8	13.7	14.9	15.0	21.5	15.36
✓	✓	✗	30.5	30.0	32.9	42.4	24.1	33.7	33.8	46.3	31.6	36.9	34.2	17.9	18.5	12.9	22.7	13.3	17.8	16.5	18.0	17.8	26.7	18.21
✓	✗	✓	30.0	31.9	32.5	44.2	24.5	34.4	35.4	43.3	31.2	38.1	34.6	17.0	19.6	11.9	19.6	14.4	16.2	15.9	18.0	18.4	26.5	17.75
✗	✓	✓	24.0	26.2	31.6	38.9	21.9	31.4	27.8	42.7	26.8	35.6	30.7	17.9	18.7	14.8	20.4	13.4	20.3	14.2	17.4	18.1	24.6	17.98
✓	✓	✓	31.6	33.8	38.3	45.7	26.4	39.7	34.5	51.4	33.8	43.1	37.8	19.1	22.0	15.1	24.2	16.7	21.0	17.2	19.5	20.9	31.1	20.68
Top-3 object Recognition Accuracy																								
✓	✗	✗	30.6	29.8	28.6	37.9	23.1	26.6	31.3	34.9	29.8	33.8	30.6	13.6	17.9	13.9	17.6	13.1	12.4	16.6	16.4	15.7	21.2	15.84
✗	✓	✗	38.8	40.1	48.7	55.3	35.7	49.5	46.5	62.6	41.9	55.5	47.5	31.5	32.2	29.1	36.1	24.6	32.8	29.0	30.7	30.1	41.9	31.80
✗	✗	✓	40.0	44.2	48.3	55.4	36.6	50.7	48.7	60.5	46.5	55.4	48.6	32.3	31.2	28.8	33.9	26.8	31.7	28.3	30.4	29.8	40.5	31.37
✓	✓	✗	53.4	51.7	56.1	66.8	43.7	56.5	55.1	66.7	53.9	62.0	56.6	34.5	34.3	29.7	38.6	28.1	34.1	30.3	31.9	33.4	45.5	34.04
✓	✗	✓	54.8	51.8	54.9	67.5	43.0	58.5	57.4	67.8	53.9	61.6	57.1	34.4	32.6	28.8	37.8	27.6	34.7	28.9	31.4	34.2	44.8	33.52
✗	✓	✓	43.4	47.7	52.4	61.2	40.3	55.5	52.2	67.0	51.2	60.8	53.2	35.8	35.8	31.2	37.8	29.1	36.5	29.9	35.0	34.3	45.9	35.13
✓	✓	✓	54.3	56.1	60.7	71.4	48.6	62.2	57.6	72.4	59.9	65.1	60.8	39.7	38.5	32.9	43.2	31.4	39.9	33.3	38.0	38.2	49.8	38.49
Top-5 object Recognition Accuracy																								
✓	✗	✗	41.6	39.8	37.2	51.1	31.6	37.9	42.4	46.1	40.7	46.3	41.5	20.1	22.6	21.0	26.0	20.8	18.9	21.4	22.7	20.9	30.1	22.45
✗	✓	✗	47.6	52.9	60.7	66.4	47.3	60.0	59.1	71.4	54.8	6												

Figure 5 shows the object recognition accuracy of Hierarchical Embedding in the full ViEEG model, while Figure 6 presents the object recognition accuracy of Hierarchical Embedding in the ViEEG model without cross-attention.

### C.1 ablation on Hierarchical Embedding

The results presented in Table 5 showcase the performance of different hierarchical EEG feature combinations on object recognition. These results were obtained from the ViEEG model with the full cross-attention mechanism.

We investigated the impact of three distinct visual embeddings:  $F_b$  (contour-based),  $F_f$  (foreground-object-focused), and  $F_r$  (contextual). Each of these embeddings contributes valuable information, but their individual contributions are limited when used in isolation.

**$F_b$ -Only (contour-based embedding)** showed moderate performance, with Top-1 accuracy ranging from 14.2% to 17.6% in the subject-dependent setting and 5.9% to 10.2 in the subject-independent setting. The contour-based features alone provide basic structure but lack the granularity needed for high accuracy.

**$F_f$ -Only (object-focused embedding)** consistently outperformed  $F_b$ -Only, with Top-1 accuracy ranging from 22.2% to 38.7% in the subject-dependent setting and 15.8% to 23.4% in the subject-independent setting. The object-focused embedding captures detailed object features, enhancing the model's ability to distinguish between classes, particularly in controlled settings.

**$F_r$ -Only (contextual embedding)** also improved performance over  $F_b$ -Only, with Top-1 accuracy ranging from 22.1% to 40.6% in the subject-dependent setting and 14.9% to 31.8% in the subject-independent setting. Contextual information helps provide broader scene understanding, aiding the model in handling more complex visual stimuli.

When combining all three embeddings ( $F_b$ ,  $F_f$ , and  $F_r$ ) as  $F_{EEG}$ , the model achieved the best results, with Top-1 accuracy reaching 34.1% to 54.0% in the subject-dependent setting and 22.7% to 31.2% in the subject-independent setting. This combination benefits from the strengths of all three feature types, with  $F_f$  contributing detailed object-level features,  $F_r$  enhancing contextual understanding, and  $F_b$  offering contour-based structural information. The complementary nature of these embeddings highlights the importance of integrating multiple types of visual information for effective EEG-based object recognition.

These findings underscore the need for a comprehensive, multi-embedding approach, where each embedding type contributes specific and essential information. Combining these embeddings leads to the most effective hierarchical feature representation, improving both subject-dependent and subject-independent recognition accuracy.

### C.2 ablation on Cross Attention

We further analyzed the effectiveness of the cross-attention module, which is essential for integrating the hierarchical features in ViEEG. Removing the cross-attention component (w/o C-Att) resulted in a noticeable performance drop. In the subject-dependent experiments, the configuration without cross-attention achieved a Top-1 accuracy of 32.4% and Top-5 accuracy of 66.8%, compared to 34.1% and 71.3% for the full ViEEG model. In the subject-independent

setting, similar trends were observed, with the full model outperforming the variant without cross-attention by significant margins. This highlights the crucial role of cross-attention in aligning and integrating hierarchical EEG embeddings, thereby improving the robustness and generalization of the model across different subjects.

The impact of cross-attention is particularly evident when integrating the different feature embeddings. As illustrated in Figure 4, the addition of cross-attention leads to significant improvements in the EEG decoding of the integrated features, especially for the following:

**Binary Mask Visual Embedding  $F_b$ :** Since this feature was not integrated or enhanced via cross-attention, its performance remains similar to the ablation results. As shown in Table 5, the Top-1 accuracy for  $F_b$ -Only is quite low, with values around 14.2% to 17.6% in the subject-dependent setting and 5.9% to 10.2% in the subject-independent setting. This shows that, without cross-attention, the feature alone is insufficient for effective object recognition.

**Foreground Object Visual Embedding  $F_f$ :** This feature benefits from contour-to-object integration, which improves performance but to a smaller extent compared to other more comprehensive features. The Top-1 accuracy for  $F_f$ -Only ranged from 22.2% to 38.7% in the subject-dependent setting and 15.8% to 23.4% in the subject-independent setting. Adding cross-attention slightly enhances its performance, demonstrating the importance of cross-attention in boosting object-specific feature extraction.

**Raw Scene Visual Embedding  $F_r$ :** This feature also shows an improvement through object-to-context integration, leading to higher accuracy compared to  $F_b$  and  $F_f$ . The Top-1 accuracy for  $F_r$ -Only ranged from 22.1% to 40.6% in the subject-dependent setting and 14.9% to 31.8% in the subject-independent setting. Cross-attention further improves this performance by aligning the raw scene features with the context, helping the model leverage broader scene information.

**Combined Binary Mask Visual Embedding  $F_{EEG}$ :** The concatenated representation of  $F_b$ ,  $F_f$ , and  $F_r$  saw the most significant improvement after adding cross-attention. As seen in the results, this combination achieved a Top-1 accuracy of 34.1% to 54.0% in the subject-dependent setting and 22.7% to 31.2% in the subject-independent setting, which is substantially higher than the individual embeddings. Cross-attention allows for the effective integration of these features, leading to a more comprehensive and robust EEG representation.

In Figure 4, we present line charts that highlight the changes in accuracy before and after the integration of cross-attention for each feature. The four subplots represent the Top-1 and Top-5 accuracy changes for each feature:  $F_b$ ,  $F_f$ ,  $F_r$ , and  $F_{EEG}$ . These subplots illustrate the performance improvements across the subject-dependent and subject-independent settings. The line charts clearly show that, although individual embeddings benefit from cross-attention, the most significant boost is observed when combining all three embeddings. This visualization allows for a clearer comparison of how cross-attention enhances the overall performance of the ViEEG model across various feature combinations. More detailed results are available in the Appendix for further reference.

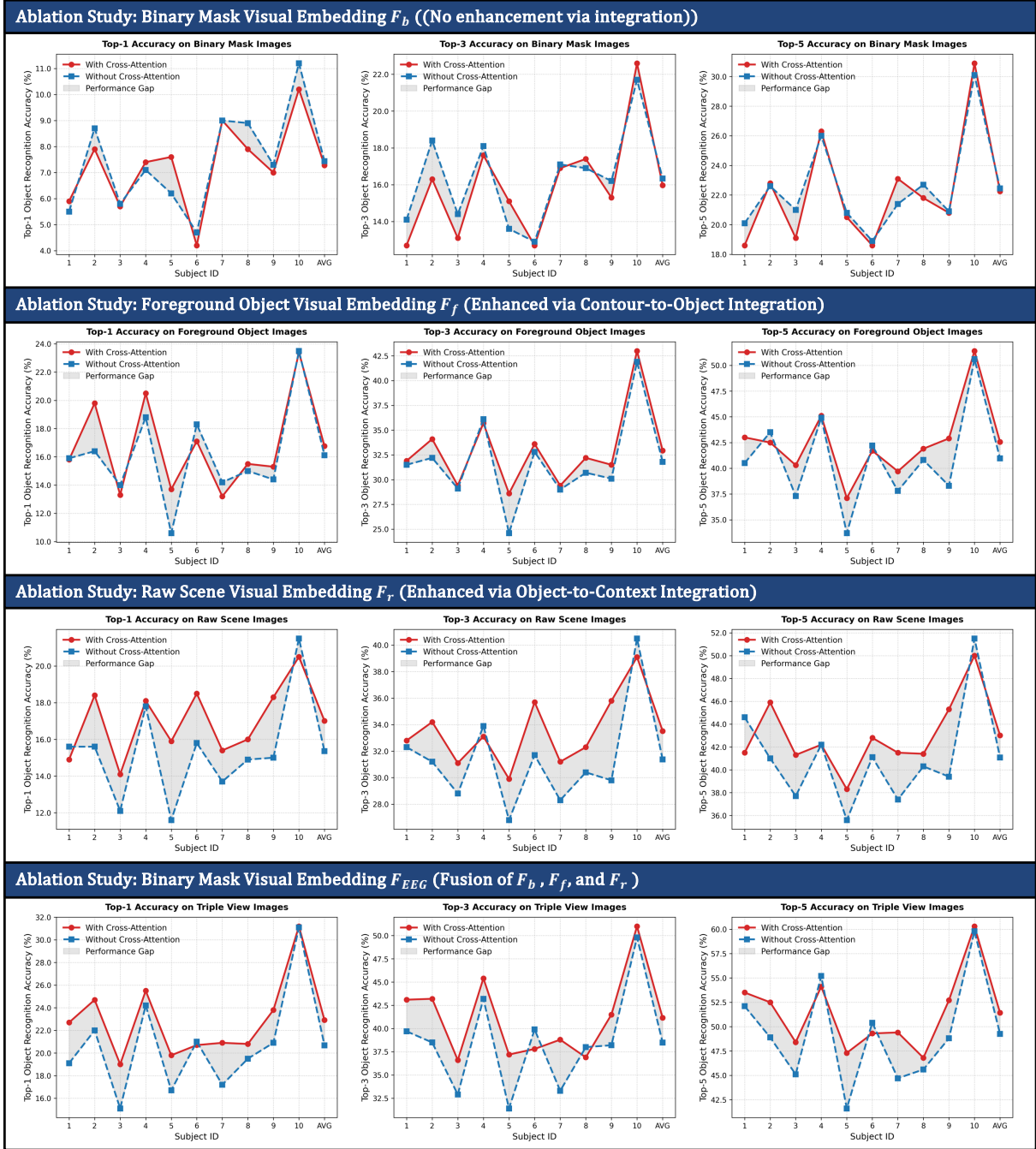
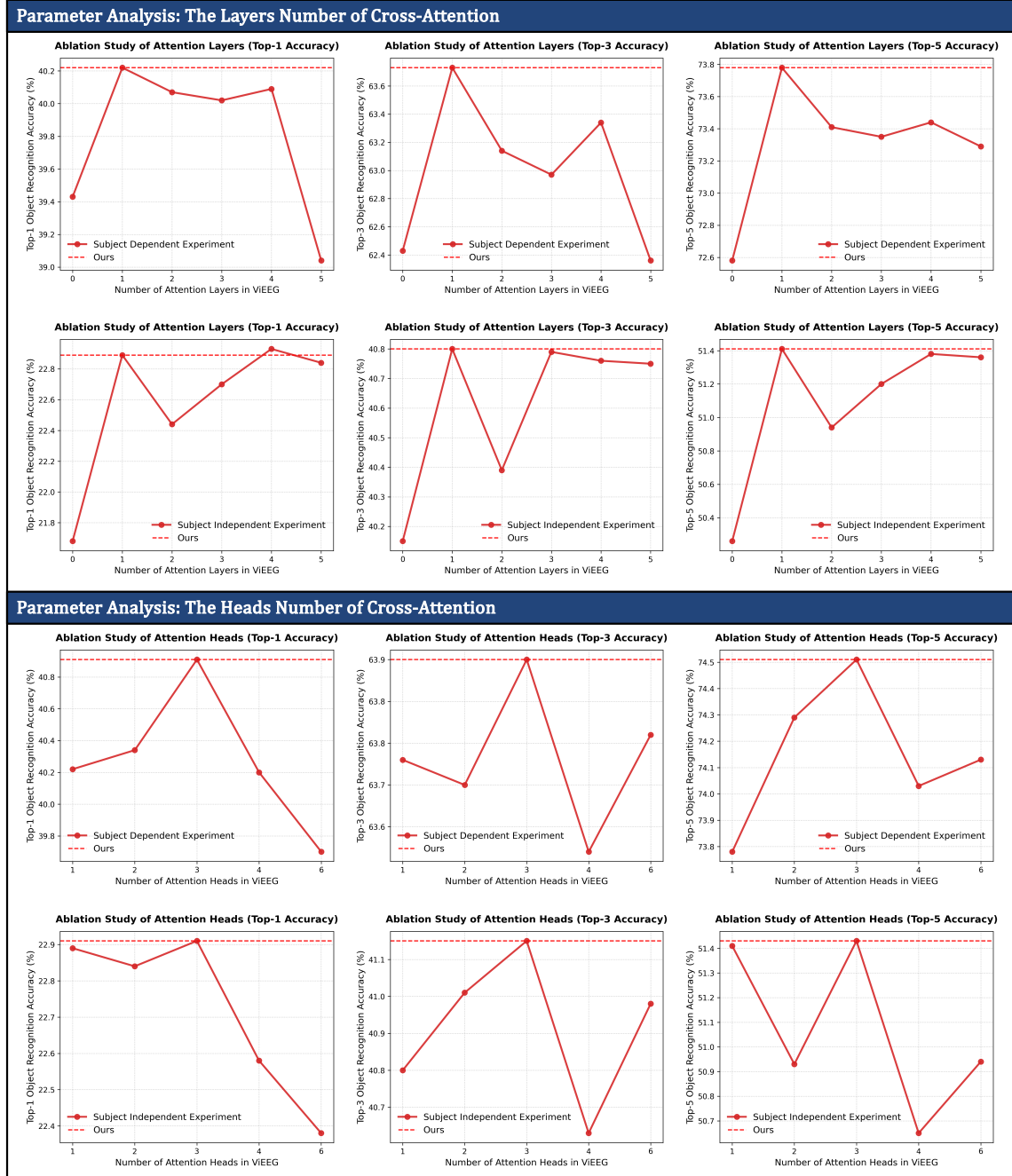


Figure 9: Detailed Ablation Study of Attention on Hierarchical Visual Embeddings in ViEEG.

### C.3 Parameter Analysis of Attention Modules

We conducted a detailed parameter analysis on the attention module in ViEEG, focusing on two key parameters: the number of attention layers and the number of attention heads. In our experiments, we recorded Top-1, Top-3, and Top-5 accuracies. For the layer analysis, we experimented with configurations ranging from 0 to 5 layers. In the within-subject object recognition task, a single attention

layer yielded the best performance, significantly outperforming the no-attention baseline. Although configurations with 3 or 4 layers occasionally produced slightly higher Top-3 and Top-5 accuracies in the cross-subject task, the performance differences were negligible while incurring a substantial increase in training parameters. Hence, we adopt a single-layer attention architecture for its optimal balance between performance and computational cost.



**Figure 10: Parameter Analysis of Attention Modules in ViEEG.** Top row: Performance trends (Top-1, Top-3, Top-5 accuracies) for varying numbers of attention layers under subject-dependent and subject-independent settings. Bottom row: Performance trends for different numbers of attention heads under the same settings.

For the head analysis, we evaluated five settings (1, 2, 3, 4, and 6 heads). While a configuration with 1 head also achieved acceptable performance, using 3 attention heads consistently provided superior results across all metrics. In the cross-subject setting, the influence of head number was less pronounced, suggesting that

the head configuration is less critical for subject-independent generalization. Overall, our findings support the use of a simplified attention module with 1 layer and 3 heads in ViEEG, effectively enhancing feature integration without unnecessary complexity.

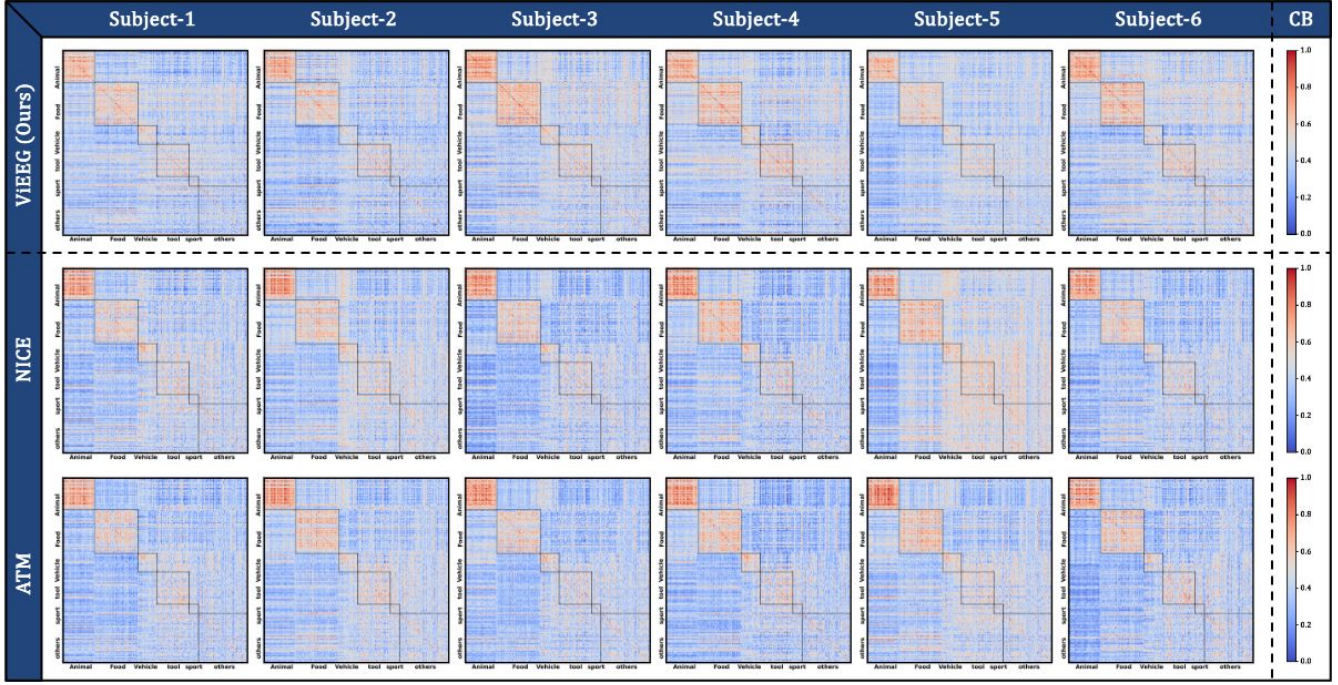


**Figure 11: Representational Similarity Matrices Across Six Subjects: ViEEG vs. NICE vs. ATM (Top: ViEEG; Middle: NICE; Bottom: ATM; CB denotes Color Bar).**

## D Model Computing Resource Comparison

Methods	FLOPs.	Param.	Avg Top-1 / Top-5 (%)
NICE	42.7354 M	2630.940 K	27.3 / 59.7
ATM	98.209 M	3072.662 K	26.1 / 58.1
CopCap	178.973 M	2954.073 K	33.3 / 60.5
ViEEG	127.973 M	7924.488 K	40.9 / 74.5

**Table 7: Comparison of model parameters, computational cost, and performance across different methods.**

Table 7 presents a comprehensive comparison of different models in terms of computational cost (FLOPs), parameter count, and recognition performance. Among the baseline methods, CopCap achieves relatively better Top-1/Top-5 accuracy (33.3% / 60.5%) but incurs the highest computational cost (178.973M FLOPs). In contrast, our proposed ViEEG achieves a significant performance gain, reaching 40.9% Top-1 and 74.5% Top-5 accuracy, outperforming all baseline methods by a large margin.

Although ViEEG has a higher parameter count (7924.488K), this increase is attributed to our self-contained hierarchical EEG encoder, which consists of spatiotemporal convolution and cross-attention modules at multiple levels. This design enables more effective extraction and integration of multi-scale EEG representations, which is crucial for capturing the complex brain responses associated with visual stimuli. Despite the higher parameter count, ViEEG maintains a reasonable computational cost (127.973M FLOPs), demonstrating a favorable trade-off between efficiency and accuracy.

## E Representational Analysis

To further support the analysis in the main text, we visualize the representational similarity matrices (RSMs) of ViEEG, NICE [31], and ATM [20] across the first six subjects from the THINGS-EEG dataset, as shown in Figure 11. Each matrix reflects how well different EEG conditions are organized in the learned representation space.

Compared to NICE and ATM, ViEEG consistently exhibits sharper diagonal structures across subjects—especially in categories with dense intra-class variation like Food and Animals—indicating better clustering and internal consistency. In contrast, categories such as Tool and Sports appear more scattered in all methods, likely due to inherent category ambiguity. This figure complements our main analysis by highlighting the stability of ViEEG across individuals.

## F Image Retrieval Results of ViEEG

To provide further insight into the effectiveness of our multi-embedding retrieval strategy, we visualize the zero-shot image retrieval results for 15 test samples from Subject 8 in the THINGS-EEG dataset. For each sample, we present the Top-10 retrieval results using four types of EEG-to-image embeddings: binary object mask (BOM), foreground object (FO), raw scene (RS), and their concatenated form (Triple embedding), as shown in Figure 12, Figure 13, Figure 14, and Figure 15, respectively.

The retrieval results reveal that each embedding modality has its own strengths under different conditions. BOM performs best when the object has simple and distinctive contours (e.g., balls,

cones), where boundary information alone is sufficient for recognition. FO excels when the object is visually entangled with the background—such as small or embedded items—where isolating the foreground is critical for accurate decoding. RS generally offers robust performance across diverse scenarios, particularly when the scene-level semantics are dominant and the image embedding is distinctive.

Most notably, the Triple embedding consistently outperforms individual modalities. This is likely due to the complementary nature of the three features—when at least one embedding retrieves a confident match, the corresponding similarity dominates the joint representation, outweighing the weaker or noisy responses from other embeddings. This fusion mechanism effectively boosts retrieval robustness and increases the likelihood of locating the correct object within the Top-5 predictions.

This multi-perspective retrieval approach is also more aligned with the way the human visual system processes complex stimuli: integrating shape, object, and contextual cues for robust perception. Overall, these results reinforce the reliability of ViEEG’s hierarchical decoding framework and highlight the advantages of combining diverse visual representations for EEG-based object recognition.

## G Image Reconstruction Results of ViEEG

### G.1 Stable Diffusion XL and IP-Adapter

To enable high-quality image reconstruction from EEG signals, we leverage Stable Diffusion XL (SDXL)[22], a state-of-the-art generative model known for its ability to produce photorealistic and semantically rich images. To bridge the modality gap between neural signals and visual content, we incorporate the IP-Adapter[38], which employs dual cross-attention modules to inject conditioning information into the denoising process. Specifically, we use CLIP-ViT-H/14 [23] to encode EEG-derived representations, enabling them to effectively influence the denoising path within the SDXL U-Net, thus guiding the model toward more precise and semantically coherent outputs.

For improved inference speed, we utilize SDXL-Turbo<sup>8</sup>, a streamlined version of SDXL optimized for rapid image generation. This variant maintains high visual fidelity while significantly reducing generation latency, making it well-suited for time-sensitive scenarios such as real-time brain signal decoding and neural interface applications.

### G.2 Additional Visualization of ViEEG’s Image Reconstruction

We present additional image reconstruction results from ViEEG on the THINGS-EEG dataset, as shown in Figure 18, Figure 17, and Figure 16. The figures illustrate the reconstruction results in three semantic categories: vehicles, food, and animals.

Overall, ViEEG successfully reconstructs images that maintain semantic consistency with the original stimuli. For example, in Figure 18 (vehicles), reconstructed images effectively capture key structural and shape features of cars, airplanes, and boats. Similarly, Figure 17 (food items) shows that ViEEG can generate food-related

textures and shapes, demonstrating its ability to retain category-level information. In Figure 16 (animals), the model reconstructs recognizable features such as fur textures and body structures, reflecting a strong alignment with the original stimuli.

However, certain semantic inconsistencies are observed in some cases. For instance, in Figure 16, when the original image is a cat, some reconstructions depict human faces. This could be due to EEG-induced associative activations, where the subject subconsciously links cats to human interactions. Additionally, errors may arise from attention fluctuations during EEG recording, leading to unintended noise in brain activity. These cases highlight potential challenges in EEG-based visual decoding, emphasizing the need for further refinement in feature alignment and reconstruction fidelity.

<sup>8</sup><https://huggingface.co/stabilityai/sdxl-turbo>

	GT Image	Top-1	Top-2	Top-3	Top-4	Top-5	Top-6	Top-7	Top-8	Top-9	Top-10
1											
2											
3											
4											
5											
6											
7											
8											
9											
10											
11											
12											
13											
14											
15											

Figure 12: Zero-shot Image Retrieval Results Using Binary Object Mask (BOM) Embeddings (Visualizations of the Top-10 retrievals for 8th Subject using binary contour-based EEG-to-image features.)

	GT Image	Top-1	Top-2	Top-3	Top-4	Top-5	Top-6	Top-7	Top-8	Top-9	Top-10
1											
2											
3											
4											
5											
6											
7											
8											
9											
10											
11											
12											
13											
14											
15											

Figure 13: Zero-shot Image Retrieval Results Using Foreground Object (FO) Embeddings (Visualizations of the Top-10 retrievals for 8th Subject using EEG features aligned with foreground object representations.)

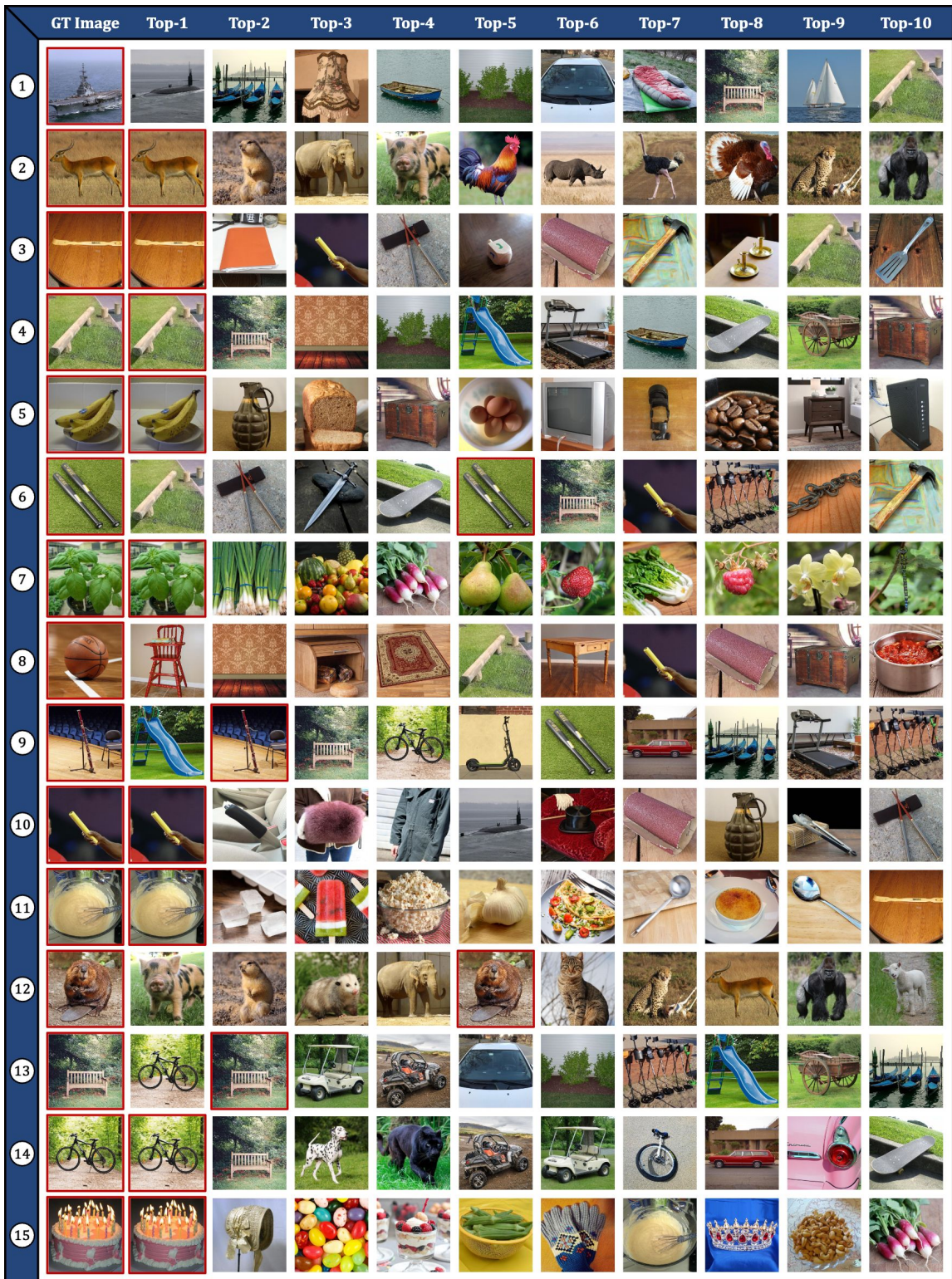


Figure 14: Zero-shot Image Retrieval Results Using Raw Scene (RS) Embeddings (Visualizations of the Top-10 retrievals for 8th Subject based on full-scene EEG-to-image alignment.)

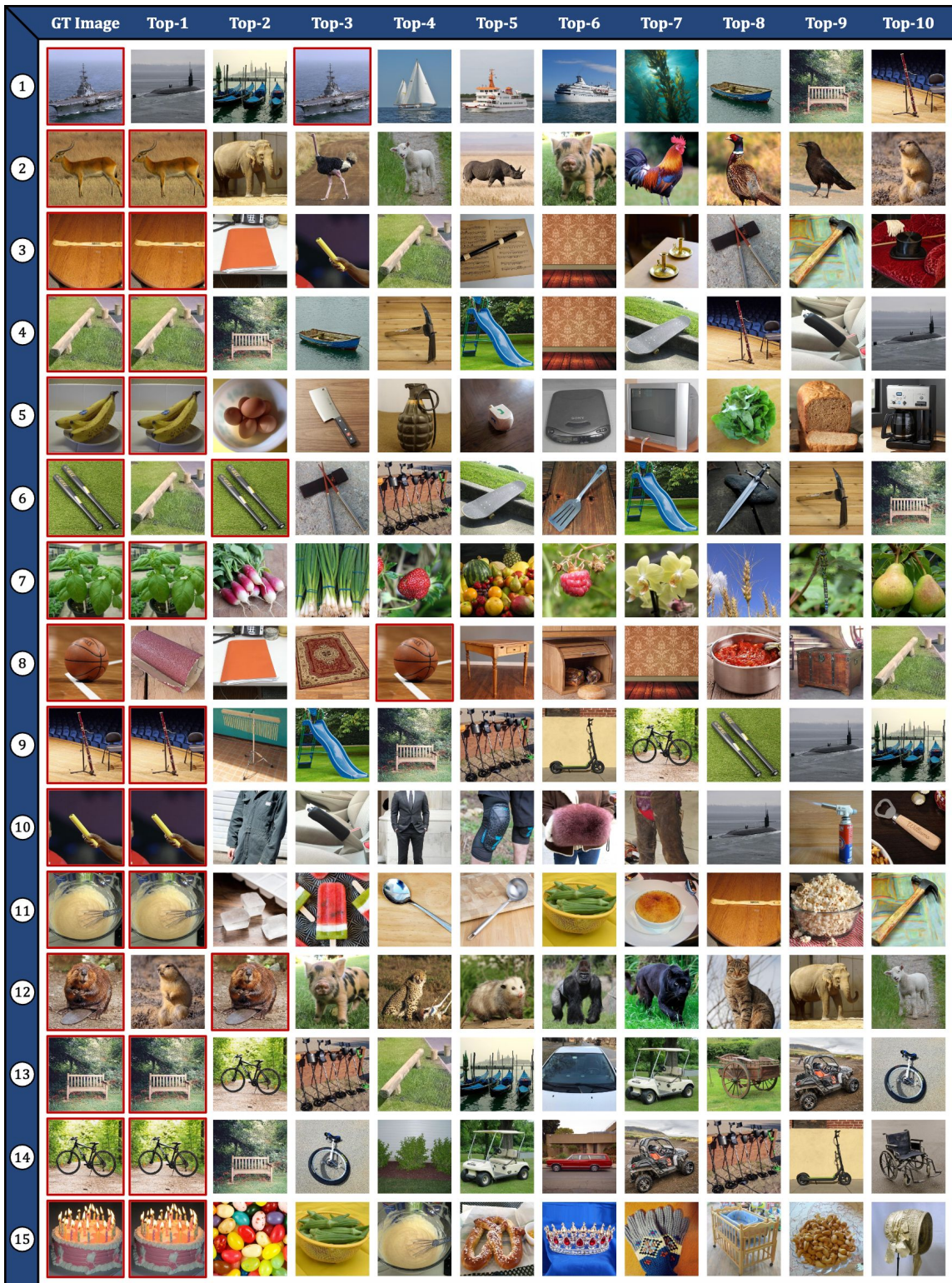


Figure 15: Zero-shot Image Retrieval Results Using Triple Embedding Fusion (BOM + FO + RS) (Visualizations of the Top-10 retrievals for 8th Subject using concatenated multi-scale EEG embeddings.)

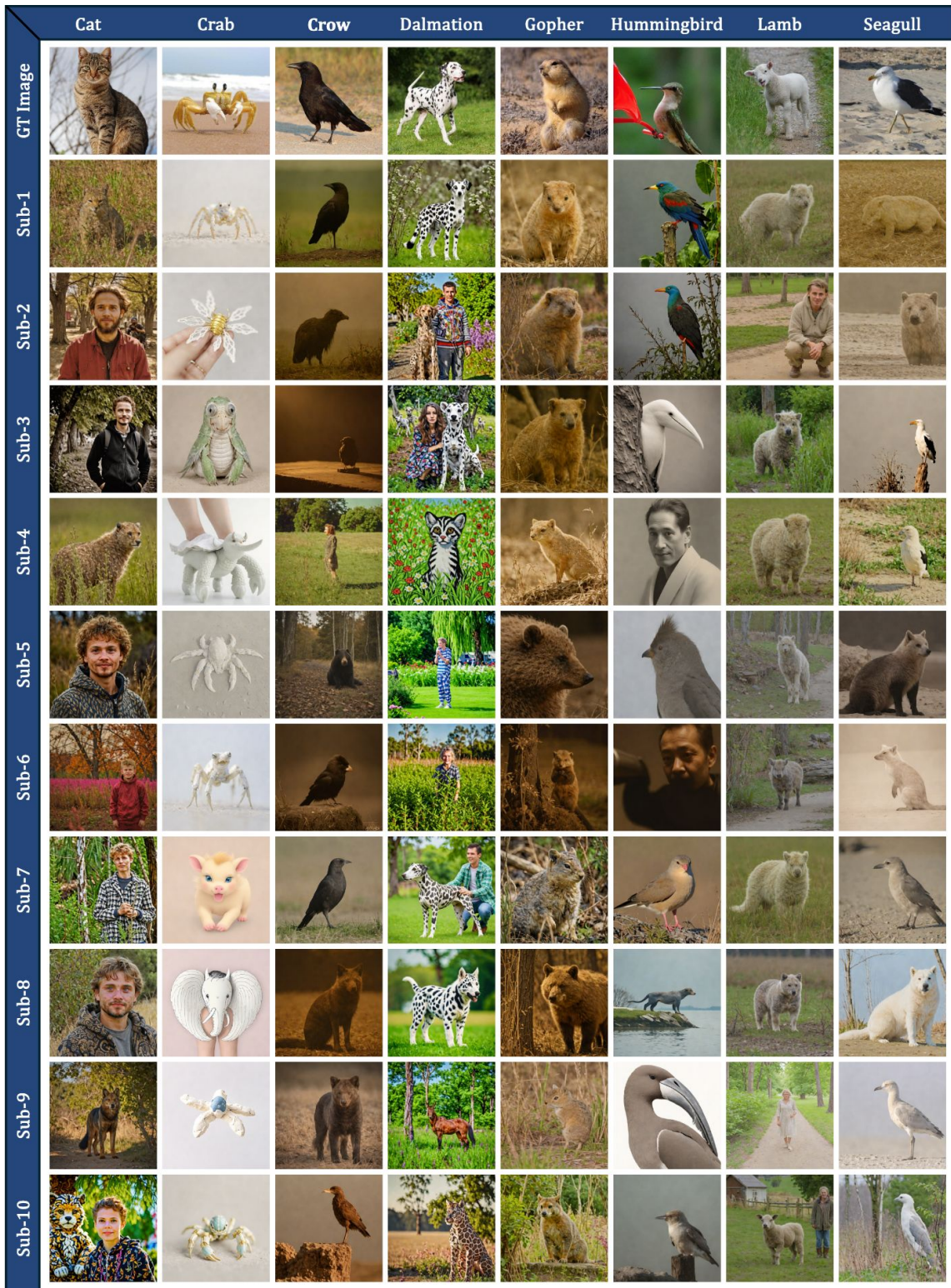


Figure 16: Reconstructed images of animal items using ViEEG.)



Figure 17: Reconstructed images of food items using ViEEG.)

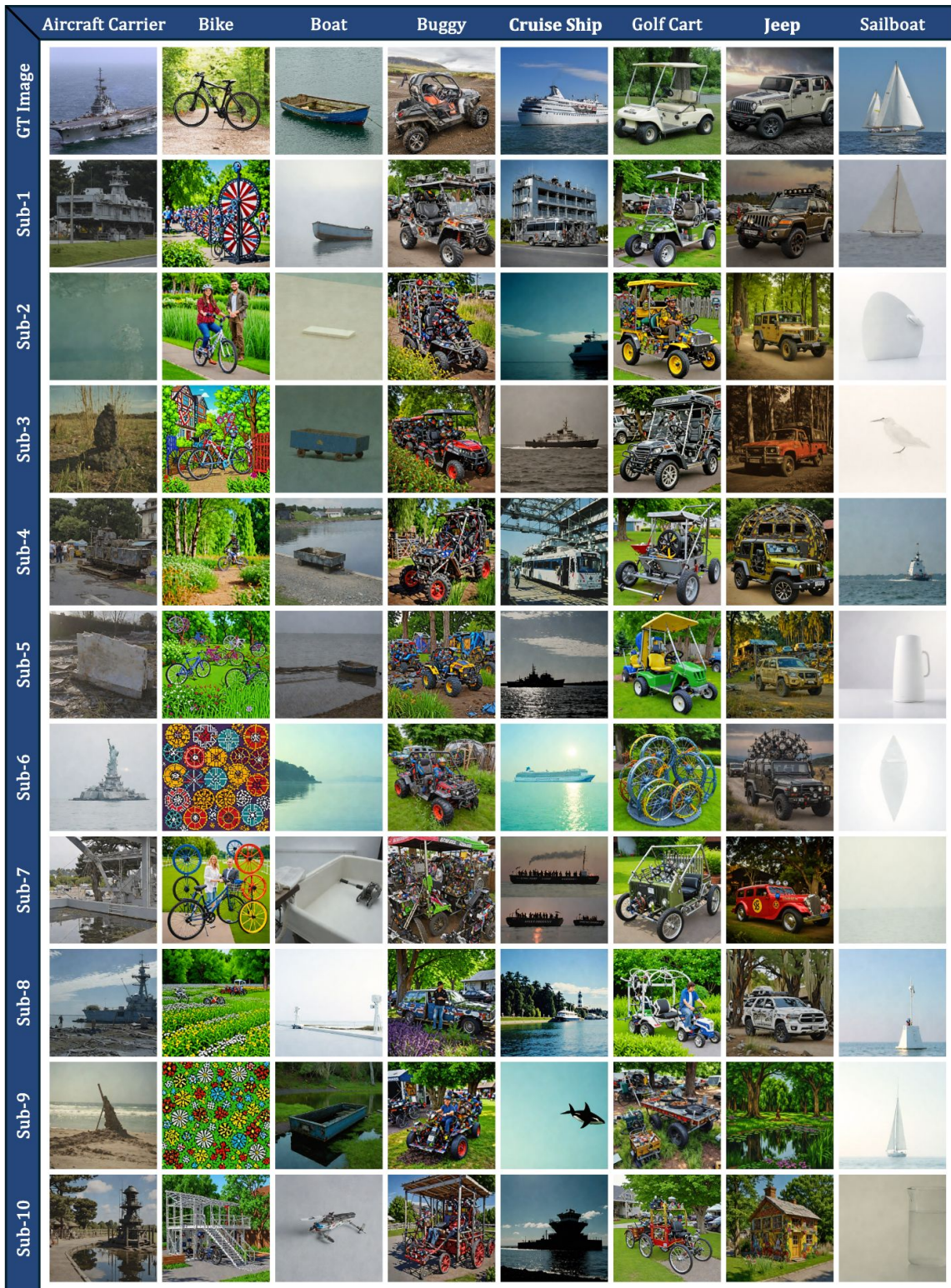


Figure 18: Reconstructed images of vehicle items using ViEEG.)